JOURNAL OF SPACECRAFT AND ROCKETS
Vol. 47, No. 4, July–August 2010

Optimal Periodic Cruise Trajectories via a Two-Level Optimization Method

Bing-nan Kang*
Northwestern Polytechnical University, 710072 Xi'an, People's Republic of China
David B. Spencer†
Pennsylvania State University, University Park, Pennsylvania 16802
Shuo Tang‡
Northwestern Polytechnical University, 710072 Xi'an, People's Republic of China
and
Dan Jordan§
Pennsylvania State University, University Park, Pennsylvania 16802

DOI: 10.2514/1.47365

The determination of optimal periodic cruise trajectories that incorporate initial states as design variables is studied in this paper. A two-level optimization method that separately deals with initial states in the outer loop and control variables in the inner loop is introduced. The outer-loop parameter optimization problem uses tradespace visualization driven by a genetic algorithm and the inner-loop optimal control problem uses the direct shooting method. A multi-objective (fuel rate and heat load) optimal periodic cruise problem in the outer loop is investigated. It is shown that if the objective of the inner loop is heat load, the fuel performance is not desirable for all the initial states. Thus, only fuel rate is the inner-loop objective. The Pareto solutions that the path constraints have no impact on control variables and that the path constraints are activated on control variables are both identified by imposing the path constraints in the outer loop and inner loop, respectively. Approximation models, built through a response surface methodology, replace the inner-loop optimization model and generate the Pareto fronts during the process of tradespace visualization.

Nomenclature

C	=	heat transfer coefficient, $\times 10^4$ kg$^{1/2}$m$^{-3/2}$
C_D	=	drag coefficient
C_{D0}	=	zero-lift drag coefficient
C_L	=	lift coefficient
C_{L0}	=	zero-angle-of-attack lift coefficient
$C_{T\max}$	=	maximum thrust coefficient
g	=	gravity acceleration of Earth, m/s^2
g_w	=	ratio of wall enthalpy to total enthalpy
h	=	altitude, m
h_{lowest}	=	lowest altitude of periodic cruise, m
h_{OSC}	=	altitude of optimal steady-state cruise, m
I_{sp}	=	specific impulsive, s
J_{OSC}	=	cost function of steady-state cruise
J_1	=	cost function of fuel-optimal periodic cruise
J_2	=	cost function of heat-optimal periodic cruise
$\bar{J}_1$	=	normalized cost function of fuel-optimal periodic cruise
$\bar{J}_2$	=	normalized cost function of heat-optimal periodic cruise
K	=	induced-drag parameter
M	=	Mach number
m	=	mass of vehicle, kg
$\dot{m}_c$	=	fuel consumption rate, kg/s
N	=	throttle node number of boost phase
n	=	acceleration load, g
$n_{\max}$	=	maximum acceleration load, g
P_j	=	angle-of-attack node number of each phase
Q	=	heat load, J/cm^2
$\dot{Q}$	=	heating rate, W/cm^2
$\dot{Q}_{\max}$	=	maximum heating rate, W/cm^2
Q_{OSC}	=	heat load of steady-state cruise, J/cm^2
$\bar{q}$	=	dynamic pressure, Pa
$\bar{q}_{\max}$	=	maximum dynamic pressure, Pa
R	=	downrange, m
R_{OSC}	=	downrange of optimal steady-state cruise, m
R_e	=	radius of Earth, m
r	=	radial distance, m
r_n	=	body nose radius, m
S_b	=	reference area for aerodynamic force, m^2
S_e	=	reference area for propulsive force, m^2
s	=	throttle
T	=	thrust of engine, N
t_{end}	=	final time of optimal steady-state cruise, s
t_f	=	period of optimal periodic cruise, s
V	=	velocity, m/s
V_{OSC}	=	velocity of optimal steady-state cruise, m/s
α	=	angle of attack, deg
γ	=	flight-path angle, deg
θ	=	downrange angle, deg
ρ	=	density of atmosphere, kg/m^3

Subscripts

f	=	final time
i	=	index of phase number
j	=	index of node number of angle of attack

Presented as Paper 2009-6285 at the AIAA Guidance, Navigation, and Control Conference, Chicago Illinois, 10–13 Aug. 2009; received 25 September 2009; revision received 7 April 2010; accepted for publication 8 April 2010.

*Ph.D. Candidate, School of Astronautics, P.O. Box 251 West Youyi Road; kbn0102@gmail.com. Student Member AIAA.

†Associate Professor, Dept. of Aerospace Engineering, 229 Hammond Building; dbs9@psu.edu. Associate Fellow AIAA.

‡Professor, School of Astronautics, P.O. Box 251 West Youyi Road; stang@nwpu.edu.cn.

§Graduate Student, Department of Aerospace Engineering, 229 Hammond Building; ddj116@gmail.com.

k = index of node number of throttle
0 = initial time

Introduction

PERIODIC cruise (PC) (as shown in Fig. 1) was first proposed in 1955 for finding fuel-optimal trajectories [1]. PC trajectories use a skipping motion and sustain this skipping motion with propulsion impulses periodically. The start point of one period is chosen when the initial flight-path angle equal to zero in this study, so that the whole trajectory can be breakup with leaving only two free variables of initial flight states (initial height h_0 and initial velocity V_0). One period of a PC trajectory then can be divided into three phases: glide phase 1, boost phase, and glide phase 2. With the propulsion in the boost phase, the vehicle flies back to the initial states at the end of one period. The widely used steady-state cruise (SC) that flies at a constant altitude and constant velocity does not satisfy the second-order Jacobi test of optimality in the frequency domain [2]. Thus, steady-state cruise does not generate fuel-optimal trajectories, although periodic cruise has not been proven to be fuel-optimal mathematically. Periodic cruise trajectories appear to achieve better fuel performance than steady-state cruise trajectories, as shown in many theoretical and numerical studies [3–10]. Two mechanisms leading to fuel efficient periodic flight have been discussed [3]. The first is that periodic cruise can make good use of the aerodynamic performance in the glide phases and thrust performance in the boost phase. Second, the vehicle may experience less drag produced by the atmosphere through the kinetic-potential energy exchange. The vehicle flies in a thinner atmosphere along the periodic cruise trajectory for the majority of time during one period. Therefore, the total energy loss can be reduced by appropriate design.

For long-range hypersonic flight, the vehicle encounters severe heating issues (total heat load and peak-heating rate). The heat load was considered as an important parameter in recent studies on periodic cruise [11,12]. The heat load generated by periodic cruise may be lower than that for steady-state cruise because the vehicle flies the majority of its time in a thinner atmosphere. However, the peak-heating rate of PC appears to be high because of the high atmospheric density in the boost phase. Thus, the peak-heating rate can be treated as a path constraint for periodic cruise [4,12].

In previous studies [3–12], the fuel rate (the ratio of the fuel consumption to the range over one period) is the only objective to be minimized. The relationship between fuel rate and heat load has not been studied extensively. The tradeoff between fuel rate and heat load with respect to design variables needs to be investigated. Also, the effects on the objectives and the path constraints from the initial flight states (h_0 and V_0) are unknown. This paper focuses on two goals: 1) generating the Pareto front of a multi-objective optimal periodic cruise (OPC) trajectory and 2) exploring the effects on the objectives and constraints from differing initial states. To compare with the OPC, optimal steady-state cruise (OSC) is also investigated in this paper. The effect of decrease of mass for OPC trajectories and OSC trajectories are both considered.

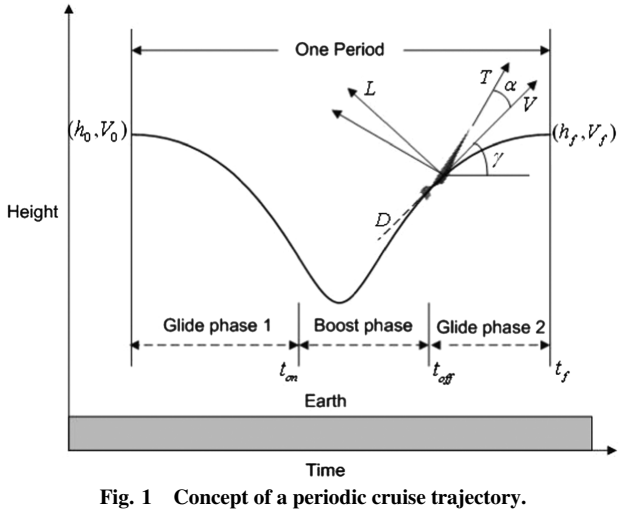

Fig. 1 Concept of a periodic cruise trajectory.

We begin by providing brief introductions to the direct method of trajectory optimization and tradespace visualization. Next, the concepts of the two-level optimization are presented. The mathematical model of optimal periodic cruise trajectories is also shown. Then, the process to solve the inner-loop nonlinear programming problem is introduced. The method to generate an initial guess of control variables of the inner-loop optimization model with different initial states is also given in this section. Then the mathematical model of optimal steady-state cruise is shown. The method to solve the OSC problem is also presented in this section. Next, the process of solving the outer-loop optimization problem via tradespace visualization is described in detail with a numerical example. The resulting costs of the OPC trajectories are compared with the costs of the OSC trajectories. The details of building the approximation model by response surface methodology is also introduced in this section. The paper then draws conclusions on the work presented.

Two-Level Optimization Method

Direct Trajectory Optimization Method

Generally, numerical methods to solve the trajectory optimization problem (optimal control problem) can be categorized into direct methods and indirect methods [13]. Direct methods discretize the original optimal control problem into a nonlinear programming (NLP) problem, and the indirect methods apply the calculus of variation (Pontryagin's maximum principle) to transfer the optimal control problem into a two-point or multipoint boundary-value problem. Indirect methods introduce the Lagrange multiplier to formulate the first-order optimality conditions. The solutions from indirect methods are closer to the true optimal solution, as compared with solutions from direct methods. However, there are some drawbacks to indirect methods [13]:

1) The initial guess is difficult to specify (generally nonintuitive).
2) The solutions are very sensitive to the initial values of multiplier variables.
3) Analytical derivatives are needed for the necessary condition.

Compared with indirect methods, direct methods are easier to converge and have more flexibility to accommodate different objectives and constraints. Thus, a direct method is used in this paper.

Direct methods can be further categorized into three groups: direct shooting, direct multiple shooting, and direct collocation. Some details of these methods can be found in [13,14]. From the view of design variables, direct multiple shooting methods and direct collocation methods also take states as design variables. Although these two methods are considered to be more robust [14], direct shooting method with the initial guess of control variables described later was found to be sufficient to solve the inner-loop optimization problem. Thus, direct shooting method is used in this study.

Tradespace Visualization

The optimization-based design can be noted as the following process [15]:

1) Formulate the design problem.
2) Develop analysis models.
3) Execute an optimization algorithm.

Although it has been studied extensively and has been applied successfully in many problems, traditional optimization-based design processes still have many shortcomings. Since the problem is many times improperly formulated, the designers are usually unsatisfied with their results. Designers are often unable to form their preferences until they see some representative optimization results [15].

Alternatively, tradespace visualization/exploration has been conceptualized to enable broad exploration of a tradespace by a decision-maker before defining the requirements, constraints, and preferences associated with a particular problem. This approach has evolved from a design-by-shopping paradigm [15], where a decision-maker

first explores a design space and then chooses an optimal solution from a set of possible designs using a visualization tool instead of relying on black box optimization algorithms. It combines expert knowledge with computational power to improve the solution by integrating multidimensional data visualization and visual steering command [16]. The following steps are associated with using tradespace visualization [17]:

1) Build a simulation model to analyze the system.
2) Run experiments.
3) Explore the tradespace by interactive visualization tools.

In this paper, Phoenix Integration's ModelCenter [18] is used to conduct the tradespace visualization. The following tradespace visualization techniques based on [19] are implemented:

1) Build the analysis model.
2) Generate the initial exploratory designs.
3) Screen design parameters; specify objectives and constraints.
4) Apply response surface methodology (metamodeling) to construct approximation model.
5) Generate the Pareto front and select the preference design.

Since the two-level optimization method is used, some unique steps (distribution of objectives and constraints, approximation model) are introduced in this paper. More detail regarding this technique will be given with an example later.

Two-Level Optimization Method

As mentioned in the introduction, one of the goals in this paper is to explore the effect on the objective and constraint from the initial states. Thus, the initial states and control variables will be handled separately. The concept of a two-level optimization method is to divide the original optimal control problem into two different subproblems: the inner-loop optimization problem is an OPC trajectory optimization problem with a given pair of $\{h_0, V_0\}$ to find the optimal control variables and to provide the values of flight parameters for inner-loop and outer-loop objectives and constraints. The outer-loop optimization problem is a parametric optimization problem to find the optimal $\{h_0, V_0\}$ by evaluating the values of flight parameters from inner loop.

The nonlinear programming problems from direct methods are often solved by local optimization algorithms (non-gradient-based or gradient-based algorithms) that can easily fall into local optimal solutions. Genetic algorithms (GAs) become a good option to increase the likelihood of finding global optimal solutions. A multi-objective GA can yield a whole set of potential solutions (generally Pareto solutions) and provide tradeoff between designs [20,21]. Each Pareto solution has the property that no other design can be found that is better in all objectives. To understand the trade between different objectives and constraints of a multi-objective (fuel rate and heat load) OPC problem, generating the Pareto front (the set of all Pareto solutions) is more meaningful than just get a pair of optimal solution. Thus, tradespace visualization driven by a GA is used to handle the initial states. However, a GA is typically insufficient in refining the solution once the general region has been identified [22], which means a GA alone is usually not sufficient to generate an accurate solution for the control variables. Also, it is shown later that the fuel performance of the periodic cruise is not desirable if the heat load is taken as the inner-loop objective: the inner loop is a single objective problem. Thus, control histories will be handled by a sequential quadratic programming (SQP) algorithm.

Hybrid methods of a genetic algorithm and a local algorithm can be categorized into two types [22–25]:

1) The solution of GA is used as the initial guess of a local algorithm [23,24].
2) A local algorithm is driven by a GA and each population of the GA is sent to the local algorithm to be local optimized [22,25].

The differences of the two-level optimization method used in this study from previous hybrid methods include the following:

1) Different algorithms (GA and SQP) deal with different design variables (initial states and control variables, respectively).
2) SQP in the inner loop is not used to refine the result of GA in the outer loop [22,25], but to provide more accurate (than GA) inner-loop solution and the values of objectives and constraints.
3) The local algorithm is not driving directly by the GA; instead, the approximation model will be introduced to speed up the searching process, as explained later.

The concept of this two-level method combining a SQP algorithm and tradespace visualization is illustrated in Fig. 2.

Figure 2 shows the relationship of the inner loop and outer loop. The function of the inner loop is to optimize the control variables with given initial states. The inputs of the inner loop are initial states from the outer loop and the outputs (for outer loop) are the values of the flight parameters for outer-loop objectives and the constraints. The function of the outer loop is to optimize initial states by evaluating the objectives and constraints from inner loop. The CFSQP [26] package is used as the inner-loop NLP solver. A multi-objective (Pareto-based) genetic algorithm so-called Darwin in ModelCenter based on a multiple elitist selection scheme [27] is used as the outer-loop solver. The selection of the GA parameters is given as follows: The initial population size is chosen to be 44, the crossover probability is 1, the mutation probability is 0.1, and the minimum change of the Pareto solutions required for improvement is 1%. If no improvement is achieved for 44 generations or a maximum 1000 generations are reached, the genetic algorithm is considered to have converged.

There are several issues raised by using the two-level optimization method:

1) Since the original optimal control problem has been divided into two suboptimization loops; how to distribute the objectives and constraints in these two loops needs to be determined.

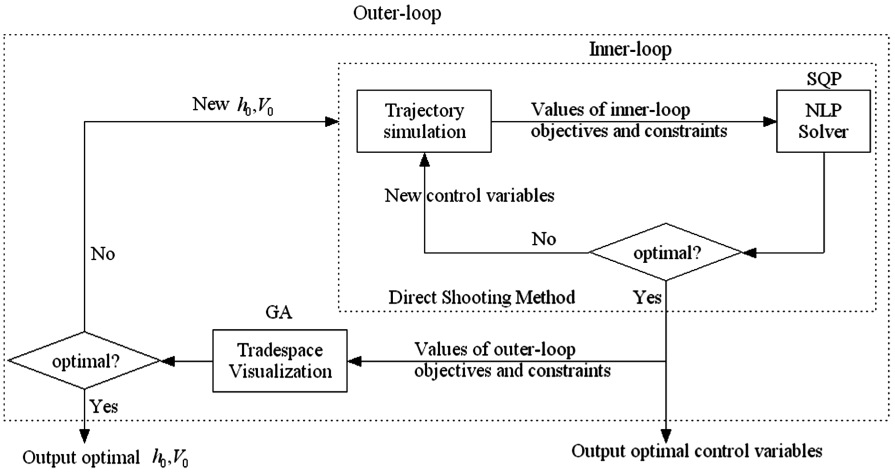

Fig. 2 Concept of the two-level optimization method.

2) A wide range of initial states will be analyzed in this paper, so a method to generate good initial guesses of the control variables under different initial states automatically is important during the tradespace visualization.

3) Each evaluation of the internal loop is actually an optimization process; how to reduce the calculation cost needs to be considered.

Optimal Periodic Cruise Problem

Problem Statement

A modified HL-20 lifting-body model [4] is used as the simulation model in this paper. The equations of motion for flight in the vertical plane over a nonrotating spherical Earth are (since the vehicle is flying in the atmosphere during its entire flight, the effects of the rotating Earth are reduced but not eliminated; because of the varying altitude and latitude, Earth rotation effects have some impact but are ignored):

$$\frac{\mathrm{d}r}{\mathrm{d}t} = V\sin\gamma \tag{1}$$

$$\frac{\mathrm{d}\theta}{\mathrm{d}t} = \frac{V\cos\gamma}{r} \tag{2}$$

$$\frac{\mathrm{d}V}{\mathrm{d}t} = \frac{1}{m}\left(T\cos\alpha - \frac{\rho S_b C_D V^2}{2}\right) - g\sin\gamma \tag{3}$$

$$\frac{\mathrm{d}\gamma}{\mathrm{d}t} = \frac{1}{mV}\left(T\sin\alpha + \frac{\rho S_b C_L V^2}{2}\right) - \left(\frac{g}{V} - \frac{V}{r}\right)\cos\gamma \tag{4}$$

$$\frac{\mathrm{d}m}{\mathrm{d}t} = -\dot{m}_c = -\frac{T}{gI_{\mathrm{sp}}} \tag{5}$$

where $m = 98830$ kg, $S_b = 250$ m^2, and $g = \mu/r^2$, and the 1976 U.S. Standard Atmosphere model is used to calculate the density of the atmosphere. The speed of sound is assumed constant and equal to 340.294 m/s. The engine model is given as follows [4]:

$$C_{T\max}(M,\alpha) = \begin{cases} 0.4736M^{1.5} + 1.6947M^{-2} & (M<4) \\ \frac{15(\alpha+5)^{0.25}}{M^{1.15}}\exp\left[-\frac{M^{0.08}}{200}\left(\alpha+5-\frac{35}{M^{0.6}}\right)^2\right] & (M\geq 4) \end{cases} \tag{6}$$

$$T = S\bar{q}C_{T\max}S_e \qquad (0\leq s\leq 1) \tag{7}$$

$$I_{\mathrm{sp}}(h,M) = \begin{cases} 4500 - 10(h-20) & (M<4) \\ -245M + 5480 - 10(h-20) & (M\geq 4) \end{cases} \tag{8}$$

where h in Eq. (8) is in kilometers. The aerodynamic model is given as follows [4]:

$$\begin{aligned} C_L(M,\alpha) &= C_{L0}(M) + C_{L\alpha}(M)\alpha \\ C_D(M,\alpha) &= C_{D0}(M) + K(M)C_L^2 \end{aligned} \tag{9}$$

$$\begin{aligned} K(M) &= 1.85[1-\exp(-0.2356M)] \\ C_{L0}(M) &= \frac{1}{20\pi}\arctan[10(M-1)] - 0.035 \\ C_{L\alpha}(M) &= 0.057\exp(-0.654M) + 0.014 \\ C_{D0}(M) &= 0.008 + 0.008\exp[-0.3(M-1.4)^2] \end{aligned} \tag{10}$$

The objective functions are the ratio of the fuel consumption to the range and total heat load over one period, and are described mathematically as

$$J_1 = \frac{\int_{t_0}^{t_f}\dot{m}_c\,\mathrm{d}t}{\int_{t_0}^{t_f}\dot{R}\,\mathrm{d}t} = \frac{m_0 - m_f}{R} \tag{11}$$

$$J_2 = \int_{t_0}^{t_f}\dot{Q}\,\mathrm{d}t \tag{12}$$

where R is given as

$$R = R_e\int_0^{t_f}\frac{V\cos\gamma}{r}\,\mathrm{d}t \tag{13}$$

The objective functions are normalized by optimal steady-state cruise (OSC) values in order to give them a more physical representation. The fuel consumption and heat load of OPC and OSC are tied to the same distance, which means

$$R_{\mathrm{OSC}} = R_{\mathrm{OPC}} \tag{14}$$

For different h_0 and V_0, the downrange of PC trajectories R_{OPC} (also R_{OSC}) is different. A higher R_{OSC} will result a higher Q_{OSC} (total heat load over R_{OSC}). Since the decrease of mass, a higher R_{OSC} will result a lower J_{OSC} (fuel rate over R_{OSC}). Thus, J_{OSC} and Q_{OSC} are different with different h_0 and V_0 of PC trajectories. The objectives, normalized fuel rate and normalized heat load, are given in Eqs. (15) and (16), respectively, as

$$\bar{J}_1 = J_1/J_{\mathrm{OSC}} \tag{15}$$

$$\bar{J}_2 = J_2/Q_{\mathrm{OSC}} \tag{16}$$

Throttle is also taken as a design variable to allow the singular arc exists in the optimal solutions [28]. As stated in the Introduction, by selecting the point when the initial flight-path angle is equal to zero as the beginning of one period, only two initial states (h_0 and V_0) are design variables. Thus, the design variables include the angle of attack $\alpha(t)$, throttle $s(t)$, start and end times of thrust (t_{on} and t_{off}), period t_f (see Fig. 1), initial height h_0, and initial velocity V_0.

The constraints include dynamic equations, path constraints, terminal state constraints, and upper/lower bound of design variables. Path constraints include maximum heating rate, maximum dynamic pressure, and maximum acceleration load. These constraints can be expressed below.

The constraint of heating rate is given as

$$\dot{Q} = C\sqrt{\rho}V^3 \leq \dot{Q}_{\max} \tag{17}$$

the heat transfer coefficient of the vehicle model used in this study is given by [4]

$$C = 1.83(10^{-8})\sqrt{r_n}(1-g_w) = 5.188(10^{-8}) \tag{18}$$

where the resulting units of heating rate are in watts per square centimeter.

The constraint of dynamical pressure is given as

$$\bar{q} = \tfrac{1}{2}\rho V^2 \leq \bar{q}_{\max} \tag{19}$$

The constraint of acceleration load is given as

$$n = \frac{\sqrt{(T\cos\alpha - D)^2 + (L + T\sin\alpha)^2}}{mg} \leq n_{\max} \tag{20}$$

For other path constraints such as structure, the load indictor (dynamic pressure–time angle of attack) can also be monitored if it was considered important. The terminal state constraints $h_0 = h_f$, $V_0 = V_f$, and $\gamma_0 = \gamma_f$ are imposed to obtain periodic trajectories. The upper/lower bounds of angle of attack, throttle, thrust time, flight time, and initial states are imposed.

Inner-Loop Optimization Model

Since the thrust is different between different phases, the optimal periodic cruise trajectory problem will be treated as a multiphase trajectory optimization problem. And the throttle $0 < s(t) \leq 1$ in the boost phase and $s = 0$ in the glide phase. Integration of states still starts from the t_0 to the t_f.

The design variables of the inner loop include the control history $\alpha(t)$ and throttle history $s(t)$, which are transformed to parametric angle of attack $\alpha_{i,j,}$ ($i = 1, 2$ and 3 and $j = 1, 2, \ldots, P_i$; there are three phases, and P_i represents the number of nodes in phase i) and parametric throttle s_k ($k = 1, 2, \ldots, N$) by the direct shooting method, start and end times of thrust (t_{on} and t_{off}), and flight time of a period t_f. All design variables are normalized to aid the convergence of the NLP solver. The total number of design variables in the inner loop is $P_1 + P_2 + P_3 + N + 3$. The terminal state constraints are considered to be fulfilled when $h_f = h_0 \pm 10$ m, $V_f = V_0 \pm 5$ m/s, and $\gamma_f = \gamma_0 \pm 0.1°$.

As mentioned earlier, providing a good initial guess for control variables under different initial states is very important. Two types of PC trajectories will be investigated here: namely, fuel-optimal PC ($\bar{J}_1$ is the objective in inner loop) and heat-optimal PC ($\bar{J}_2$ is the objective in inner loop). The maximum-glide trajectory makes good use of the aerodynamic performance of the vehicle, so the initial value of the angle of attack for the fuel-optimal periodic cruise trajectories can be given from maximum-glide trajectories. Since maximum lift/drag ratio L/D trajectories are near-maximum-glide trajectories and the expression of $\alpha_{\max L/D}$ can be given analytically, $\alpha_{\max L/D}$ will be used as initial guess of angle of attack for fuel-optimal PC trajectories. With the definition of maximum L/D trajectory, we have

$$\left[\frac{\partial}{\partial\alpha}\left(\frac{L}{D}\right)\right]_{\max L/D} = 0 \tag{21}$$

Substitute Eq. (9) in Eq. (21), $\alpha_{\max L/D}$ can be given as

$$\alpha_{\max L/D} = \frac{1}{C_{L\alpha}}\sqrt{\frac{C_{D0}}{K}} - \frac{C_{L0}}{C_{L\alpha}} \tag{22}$$

One key issue in implementing the two-level optimization method efficiently is to give a good initial guess of t_{on}, t_{off}, and t_f with different initial states. The guess of these three variables for fuel-optimal PC trajectories will be given by the following two steps:

1) Generate the maximum L/D trajectory. Track the time at the lowest height $t_{\text{on}_{\text{guess1}}}$ and flight time $t_{f_{\text{guess1}}}$.

2) Pass the $t_{\text{on}_{\text{guess1}}}$, $t_{f_{\text{guess1}}}$, and $t_{\text{off}_{\text{guess1}}} = t_{\text{on}_{\text{guess1}}} +$ constant values to generate an optimal periodic cruise trajectory via the SQP algorithm.

For given initial states, it can be expected that the main difference between the powered fuel-optimal periodic cruise trajectory and the unpowered maximum L/D trajectory is the segment after t_{on}. Also, the thrust initiation should be close to the lowest altitude because lower altitude will benefit the specific impulse, I_{sp} of the engine, as shown in Eq. (8). So the time of lowest altitude of the maximum L/D trajectory $t_{\text{on}_{\text{guess1}}}$ can be a good guess of t_{on}. The time when the trajectory reaches the next peak (the flight-path angle is zero) is considered to be the flight time of the unpowered maximum L/D trajectory $t_{f_{\text{guess1}}}$. These initial guesses are then passed to the SQP algorithm.

For heat-optimal PC trajectories, a higher mean altitude results in a lower heat load. To improve the altitude of a PC trajectory (for given initial states), a higher angle of attack and a longer thrust time are desirable. Thus, initial guess for heat-optimal PC trajectories is unpowered glide trajectories with a high angle of attack. The time when the trajectory reaches the next peak (the flight-path angle is zero) is considered to be the flight time of the unpowered high-angle-of-attack trajectories $t_{f_{\text{guess2}}}$. The initial guess of thrust start time $t_{\text{on}_{\text{guess2}}} = 0$, and the initial guess of thrust end time $t_{\text{off}_{\text{guess2}}} = t_{f_{\text{guess2}}}$. The numerical results show that these methods are quite robust and efficient with a wide range of initial states. However, the inner-loop optimization problem will produce a response surface biased towards those initial guess trajectories and, thus, the search of the GA is confined to those trajectories represented on the surface. A true global search of the design space in the inner loop is not conducted.

Optimal Steady-State Cruise Problem

To compare with the optimal periodic cruise, the optimal steady-state cruise is also studied. The fuel rate in Eq. (11) is minimized subject to steady-state dynamic equations. Since the altitude and velocity are constant during the flight of SC trajectories, the steady-state dynamic equations that contain angle of attack and throttle can be given from Eqs. (3), (4), and (7) as follows:

$$s\bar{q}C_{T\max}S_e\cos\alpha - \frac{\rho S_b C_D V^2}{2} = 0 \tag{23}$$

$$s\bar{q}C_{T\max}S_e\sin\alpha + \frac{\rho S_b C_L V^2}{2} - m\left(g - \frac{V^2}{r}\right) = 0 \tag{24}$$

There is no glide phase for this type of trajectory (there will be no t_{on} and t_{off}). The final time t_{end} will be determined by corresponding OPC trajectory to be normalized: t_{end} is the time when Eq. (14) is satisfied. Thus, the free design variables of OSC problem include $\alpha(t)$, $s(t)$, h, and V. The OSC problem can expressed by

$$\min_{\alpha(t),s(t),h,V} J_{\text{OSC}}$$

The instantaneous α and s can be solved numerically from Eqs. (23) and (24) if the altitude and velocity are known. Thus, the OSC problem can be divided into two subproblems (the structure of these two subproblems is similar to the two-level structure of OPC problem):

1) The inner loop of OSC problem is to find the angle of attack and throttle that satisfy the steady-state equations by the Newton–Raphson method.

2) The outer loop of OSC problem is to find the initial altitude h_0 and initial velocity V_0 to minimize the cost (fuel rate) by the genetic algorithm in ModelCenter.

Different from the OPC two-level structure, the inner loop of OSC problem is not an optimization process but a root-finding problem. Since the decrease of mass is considered, the instantaneous α and s of OSC from Eqs. (23) and (24) will be used to integrate Eqs. (1–5). The histories of altitude, velocity, and mass of steady-state cruise are solved numerically. The altitude and velocity will equal to h_0 and V_0 as long as the integration step is small. The angle of attack and throttle will change along with the flight, since the mass of the vehicle decreases. The result of OSC problem will be given in the next section.

Numerical Result

Optimal Steady-State Cruise

Figures 3 and 4 show the results of OSC trajectories with different final time t_{end}. Since the decrease of the vehicle mass, the mean value of the vehicle mass is lower for longer t_{end}. The fuel rate is lower for the same vehicle model with lower mass. Thus, the fuel rate decreases for longer t_{end} and the heat load increases for longer t_{end}, as shown in Fig. 3. The h_{OSC} and V_{OSC} are slightly higher for longer t_{end}, as shown in Fig. 4.

Figure 5 shows the fuel rate versus altitude and velocity of the steady-state cruise trajectories with $t_{\text{end}} = 238.65$ s (this OSC trajectory is used to normalize the fuel-optimal PC trajectory without path constraints from $h_0 = 55$ km and $V_0 = 5000$ m/s, shown later). The solution of the optimal steady-state cruise trajectory solved by a genetic algorithm is $h_{\text{OSC}} = 43.07$ km, $V_{\text{OSC}} = 4956.4$ m/s, $R_{\text{OSC}} = 1174.18$ km, and $J_{\text{OSC}} = 1.5305$ kg/km (fuel rate).

Figure 6 shows the histories of angle of attack and throttle of the OSC trajectory. It is shown that the angle of attack and throttle will decrease slightly along with the flight, since the mass decreases.

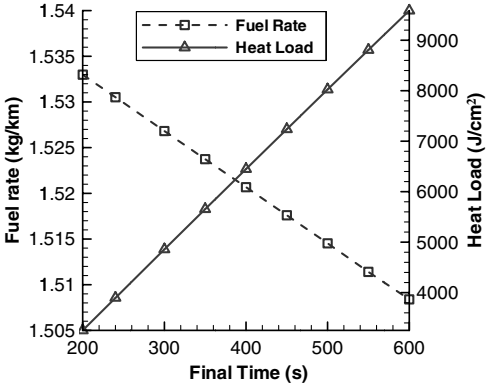

Fig. 3 Fuel rate and heat load of OSC trajectories with different final times.

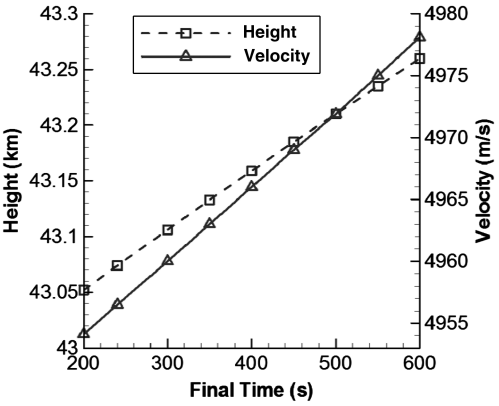

Fig. 4 Height and velocity of OSC trajectories with different final times.

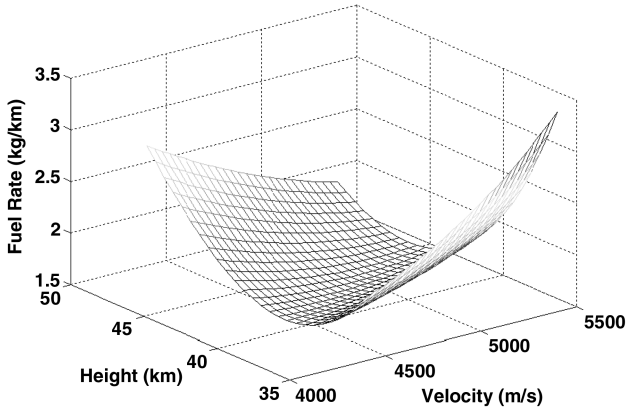

Fig. 5 Fuel rate of steady-state cruise versus altitude and velocity ($t_{\text{end}} = 238.65$ s).

Optimal Periodic Cruise of Inner Loop

The inner-loop optimal periodic cruise trajectories ($h_0 = 55$ km, $V_0 = 5000$ m/s) with different objectives and path constraints are analyzed here. The node numbers are given as $P_1 = P_3 = 11$ and $P_2 = N = 6$ for the fuel-optimal PC trajectory without path constraints, $P_1 = P_3 = 2$ and $P_2 = N = 21$ for heat-optimal PC trajectory, and $P_1 = P_2 = P_3 = N = 10$ for the fuel-optimal PC trajectory with path constraints ($\dot{Q}_{\max} = 500$ W/cm^2 and $n_{\max} =$ 2 g). The bounds of control variables are $0 \le \alpha(t) \le 20$ deg and $0 \le s(t) \le 1$. The downrange of these PC trajectories are $R_{\text{OPC}} = 1174.18$, 1187.63, and 1183.88 km. The fuel rate and heat load of this PC trajectory will be normalized by the OSC trajectories

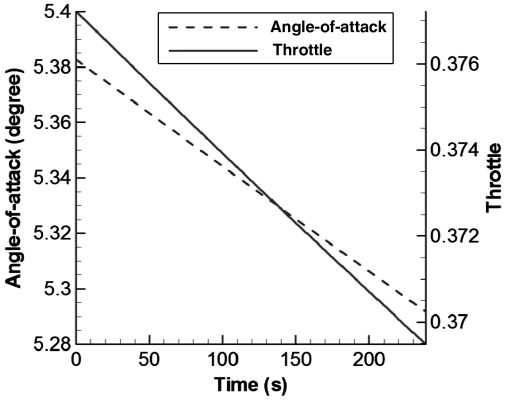

Fig. 6 Control variables of OSC trajectory ($t_{\text{end}} = 238.65$ s).

with $t_{\text{end}} = 238.65$, 241.36, and 240.61 s. The control variables of the OPC trajectories are given in Figs. 7–9.

Figures 7–9 show that for the model used in this paper, the throttle will follow a bang–bang control structure for all these OPC trajectories. Thus, the throttle can be set to 1 in the boost phase. The altitudes of the OSC trajectory and the OPC trajectories are given in Fig. 10. It can be seen from Fig. 10 that for given initial states, imposing path constraints will increase the altitude of PC trajectories. The heat-optimal PC trajectories tend to fly as high as possible to reduce the heat load. However, this will increase the fuel rate significantly, since the engine is on for the majority time (full period in this case) of one period, as shown in Fig. 8.

Two factors need to be considered when choosing node numbers of design variables: calculation cost and precision. Table 1 shows the result of different node numbers of angle of attack and throttle for a

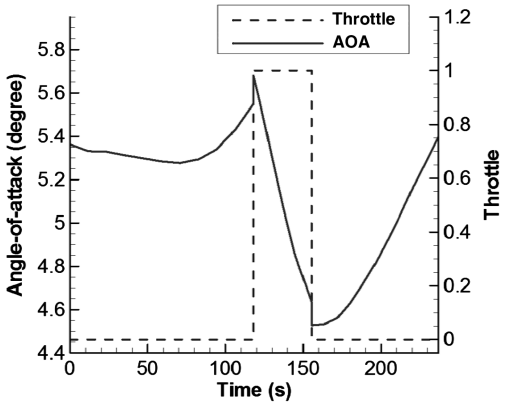

Fig. 7 Control variables of fuel-optimal PC trajectory without path constraints.

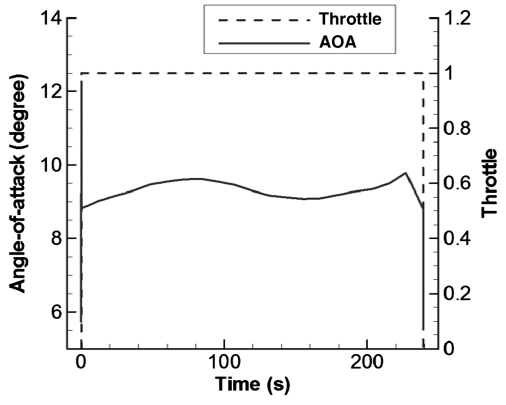

Fig. 8 Control variables of heat-optimal PC trajectory.

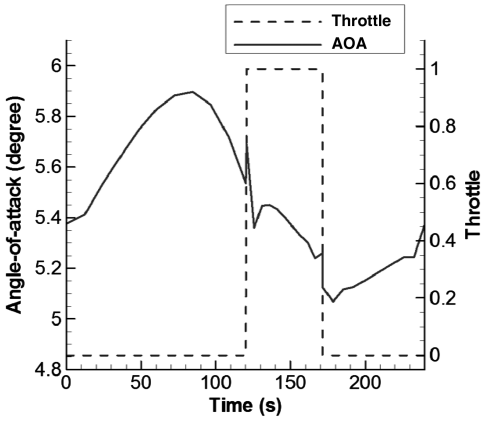

Fig. 9 Control variables of fuel-optimal PC with path constraints.

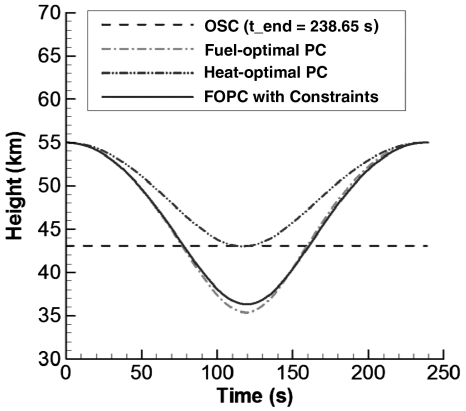

Fig. 10 Altitude of OSC trajectory and OPC trajectories (FOPC denotes fuel-optimal PC).

fuel-optimal periodic cruise trajectory ($h_0 = 55$ km and $V_0 =$ 5000 m/s) with given optimal t_{on}, t_{on}, and t_f.

Table 1 shows that more nodes of angle of attack may result in a better solution (the difference is less than 0.5%) but significantly higher calculation cost. The design variables t_{on}, t_{off} and t_f have more influence on the objectives than the number of angle-of-attack nodes. Two nodes in each phase can generate near-optimal solutions from the numerical test. Thus, the effect of node number of angle of attack is ignored and the number of nodes in each phase was chosen to be two in the process of tradespace visualization to reduce the calculation cost.

Determination of Inner-Loop Objectives and Constraints

The first step of tradespace visualization is to build an analysis model [19]. The model used in this paper is the inner-loop optimization program that generates the periodic cruise trajectories. We still need to determine the objectives and constraints of the inner-loop optimization to complete building the analysis model.

Determination of Objectives in the Inner-Loop

Experimental designs are often used to explore the design space and get better understanding of the effect of input (factor) on output (response). The sample data generated from an experimental design can also be used to construct an approximation model. An experimental design is expressed in terms of factors (design variables) set at specified levels (value of design variables) [29]. A survey of experimental designs can be found in [29]. The most basic experiment is a full factorial experiment that specifies levels for each factor and evaluates the outputs at every combination of the values. Since there are only two design variables (h_0 and V_0) in the outer loop, the number of runs for a full factorial experiment is acceptable. To determine the objective of the inner loop, two full factorial experiments (2 factors at 21 levels) are conducted, where the objective is optimal fuel rate $\bar{J}_1$ and optimal heat load $\bar{J}_2$. The upper boundary of initial height is constrained to 120 km (altitude of reentry interface). The lower boundary is constrained to 50 km (higher than h_{OSC}). The range of velocity is from 4500 to 6000 m/s. The results of these two experiments are given in Figs. 11–14.

Figure 12 shows that if the objective of the inner loop is $\bar{J}_1$, the majority fuel-optimal PC trajectories can still achieve better heat performance than the OSC trajectory while maintaining low fuel rate as well (see Fig. 11). On the other hand, if the objective of the inner loop is $\bar{J}_2$, the lowest resulting normalized fuel rate is 1.1, as shown in Fig. 13, which means cost more fuel than the OSC trajectory, though the heat load is low (see Fig. 14). The results from the second experiment are not desired for OPC trajectories. It is more difficult to get a lower fuel rate compared with a lower heat load. Thus, we consider the fuel rate be the only objective in the inner-loop optimization.

Determination of Constraints in the Inner-Loop

Once we determined the inner-loop objective, the next step is to determine the path constraints of the inner loop (dynamic equations, terminal state constraints, and upper/lower bound of design variables should be imposed on the inner loop to generate periodic cruise trajectories). From the experimental design, it can be seen that different initial states result in the variance of maximum heating rate from 422.64 to 1425.42 W/cm^2. The maximum acceleration load varies from 0.662 to 9.67 g. The maximum dynamic pressure varies from 33.55 to 489.79 KPa. The different values of these constraints on given initial states (55 km, 5000 m/s) are imposed to test the effects on the path constraints from the control variables. The results are given in Figs. 15–17.

Compared with the variance of the maximum heating rate constraint achieved by the initial states, the one achieved by the control variables (angle of attack, throttle, thrust times, and flight time) is relatively small. On the other hand, Figs. 15–17 show that constraining the path constraints through the control variables will degrade the fuel-rate performance but improve the heat performance

Table 1 Results with different node numbers for OPC trajectories

Node number (P_1-P_2-P_3)	Fuel rate, normalized	Heat load, normalized	Calculation time, s
	Fuel-optimal PC (no path constraints)		
2-2-2	0.93271	1.00604	6
11-11-11	0.93265	1.00437	59
21-21-21	0.93265	1.00433	157
	Heat-optimal PC		
2-2-2	1.17038	0.51147	10
2-11-2	1.17033	0.51113	101
2-21-2	1.17035	0.51112	226
	Fuel-optimal PC with path constraints		
2-2-2	0.93806	0.92703	23
11-11-11	0.93771	0.93293	100
21-21-21	0.93771	0.93282	228

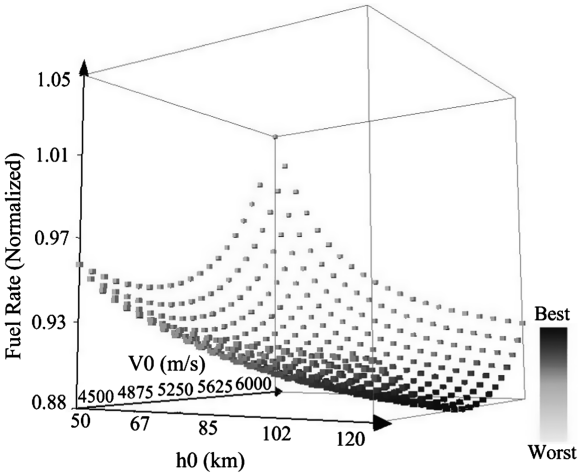

Fig. 11 Experimental design space of fuel-optimal PC trajectories of the inner loop: fuel rate (shade reflects the change of fuel rate).

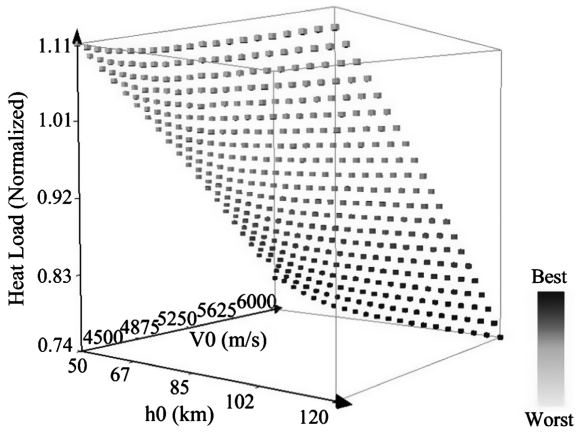

Fig. 12 Experimental design space of fuel-optimal PC trajectories of the inner loop: heat load (shade reflects the change of heat load).

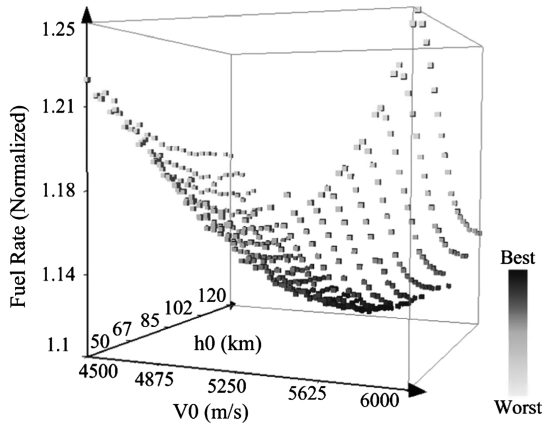

Fig. 13 Experimental design space of heat-optimal PC trajectories of the inner loop: fuel rate (shade reflects the change of fuel rate).

(except for maximum acceleration load case shown in Fig. 16). For example, when the maximum heating rate of 400 W/cm^2 is imposed, the value of normalized fuel rate increases to 1.015 (which is even worse than the optimal steady-state cruise trajectories) and the value of normalized heat load reduces to 0.686. From Figs. 15–17, we can also see that imposing a small constraint in the inner loop will not degrade the fuel rate significantly and reduce the heat load. Applying small constraints through the control variables can widen the search space for the initial states (relax the constraints on the initial states). Thus, the results without and with the inner-loop path

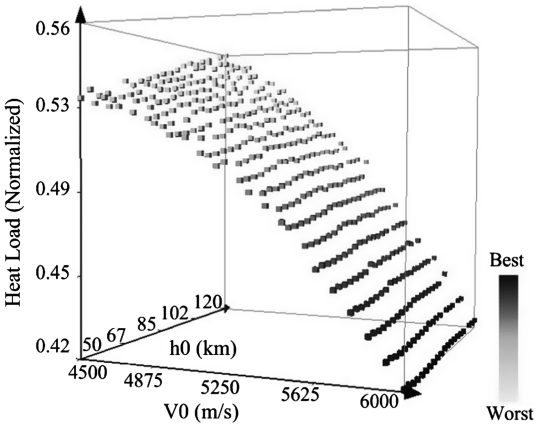

Fig. 14 Experimental design space of heat-optimal PC trajectories of the inner loop: heat load (shade reflects the change of heat load).

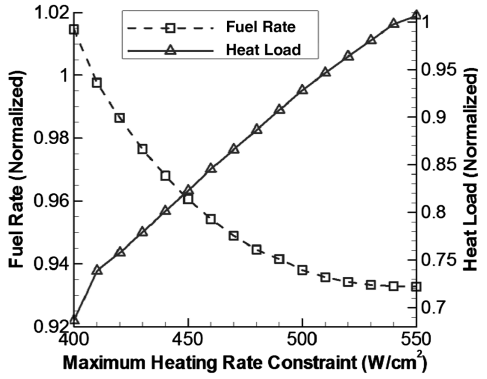

Fig. 15 OPC with different maximum heating rate constraints (55 km, 5000 m/s).

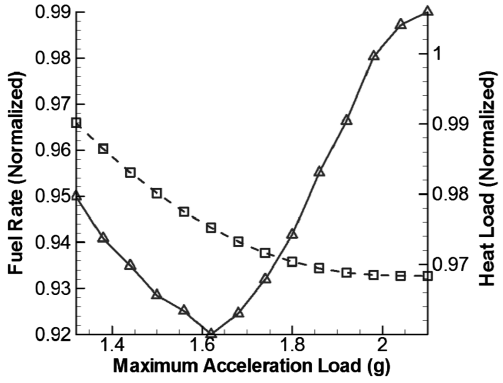

Fig. 16 OPC with different maximum acceleration load constraints (55 km, 5000 m/s).

constraints will be both investigated. The $\dot{Q}_{\max}$ and $n_{\max}$ are considered as the inner-loop path constraints, since the effects of $\dot{Q}_{\max}$ and $\bar{q}_{\max}$ are similar, as shown in Figs. 15 and 17. The tradespace visualization without the inner-loop path constraints will be first analyzed next.

Generation of Initial Exploratory Designs

Once the inner-loop objectives and constraints are determined, the analysis model has been built for the tradespace visualization. The exploration of the full design space can then be conducted with the inner-loop optimization model. The results of the path constraints are given in Figs. 18–20 (the results of the objective are already shown in Figs. 11 and 12). Also, we can identify some trends in the data and find some relationships between the inputs and outputs.

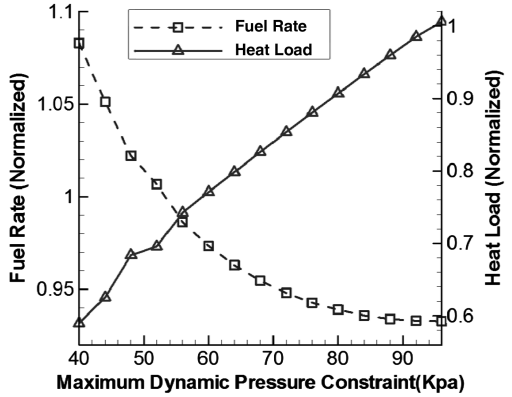

Fig. 17 OPC with different maximum dynamic pressure constraints (55 km, 5000 m/s).

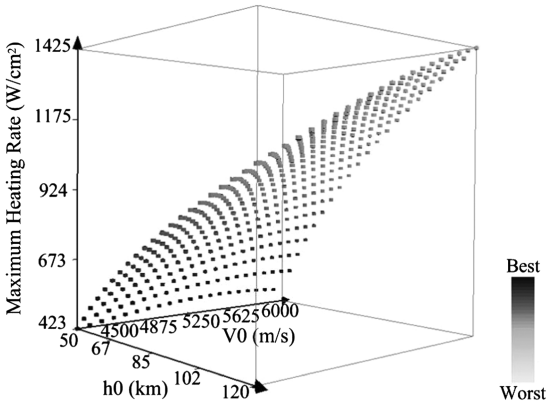

Fig. 18 Experimental design space of fuel-optimal trajectories of the inner loop: maximum heat rate (shade reflects the change of $\dot{Q}_{\max}$).

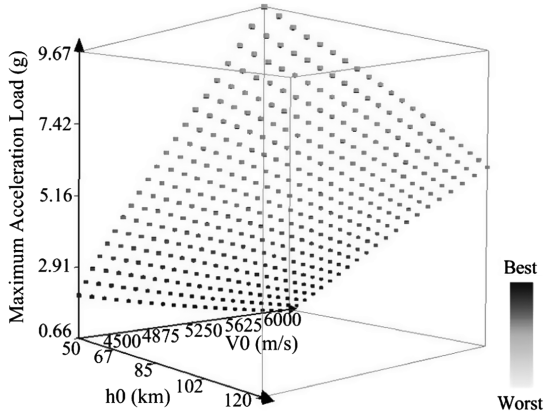

Fig. 19 Experimental design space of fuel-optimal trajectories of the inner loop: maximum acceleration load (shade reflects the change of $n_{\max}$).

Figure 11 shows that the normalized fuel rate varies from 0.883 to 1.054. A higher h_0 can achieve a lower fuel rate. For each h_0, there exists a fuel-optimal V_0. The value of this V_0 increases as h_0 is higher. To analyze the mechanism of the fuel rate with respect to h_0 and V_0, two factors should be considered: the drag effect for a given range and the engine performance. Since the optimal angle of attack makes good use of the aerodynamic performance of the vehicle, only the flight environment (dynamic pressure) factor of the drag effect is considered. For a given V_0, a higher h_0 can make most parts of the flight altitude higher (beginning and ending part) and only a small part of flight altitude lower (middle part). From the numerical results, the drag effect is reduced for a given range by using a higher h_0. The engine performance is improved because of the lower altitude in the boost phase can benefit I_{sp} of the engine, as shown in Eq. (8). Thus, lower fuel consumption is achieved. For a given h_0, a higher V_0 will keep the entire flight higher. Here, the drag effect for a given range is reduced. However, the engine performance is degraded due to higher altitude in the boost phase. That is the reason there is an optimal V_0 for given h_0, which has the best balance between drag effect and engine performance.

Figure 12 shows that the normalized heat load varies from 0.735 to 1.11. A higher h_0 and a higher V_0 will cause a lower heat load. The V_0 dominates the variance of heat load, and the optimal heat load solutions tend to have highest V_0. For a given h_0, a higher V_0 will keep the vehicle flight higher and longer. Though the flight velocity is higher, the effect from lower atmospheric density is more significant. The total heat load for a given range is reduced by increasing V_0. For a given V_0, a higher h_0 can make part of flight height higher (the glide phases) but make other parts of flight height lower (the boost phase). The total effect of increasing the h_0 can slightly reduce the total heat load for a given range.

Figures 18–20 show that for a given V_0, a higher h_0 will cause a higher $\dot{Q}_{\max}$, $n_{\max}$, and $\bar{q}_{\max}$. This is because a higher h_0 will cause a lower h_{lowest}, which means the atmospheric density will be higher (the velocity at h_{lowest} are approximately the same). Thus, $\dot{Q}_{\max}$, $n_{\max}$, and $\bar{q}_{\max}$ will increase. For a given h_0, a higher V_0 will cause a lower $n_{\max}$ and $\bar{q}_{\max}$ but a higher $\dot{Q}_{\max}$. This is because increasing V_0 will cause a higher velocity at h_{lowest} and a higher h_{lowest} (lower atmospheric density). There will be a tradeoff effect on these constraints when V_0 increases. The effect of velocity on maximum heating rate is a more significant effect according to Eqs. (17), (19), and (20).

Screen Design Parameters

The next step is to specify the objectives and constraints for the outer-loop (the constraints in the outer-loop include path constraints and upper/lower bound of design variables). From Figs. 11 and 12, the trends of fuel rate and heat load are very different. These two competing objectives form a trade off. So the outer-loop objectives include fuel rate and heat load. Since the acceleration load is related to the dynamic pressure, as shown from Figs. 19 and 20, we only consider the maximum acceleration load and maximum heating rate constraints in the outer loop. Once the path constraints are imposed, the distribution of the optimal solutions will be changed. So the goal of the tradespace visualization is to determine the optimal solutions subject to different path constraints.

To observe the effect on the objectives from the path constraints, contour plots of fuel rate and heat load are given in Figs. 21 and 22, respectively (the units of $\dot{Q}_{\max}$ are W/cm^2 and the unit of $n_{\max}$ is g in the contour plots). The path constraints are approximated by straight lines. The numbers beside the shade bar are the value of normalized fuel rate and normalized heat load in Figs. 21 and 22, respectively.

Figure 21 shows once the path constraints are imposed, the highest height of the feasible area is the height on the intersection of

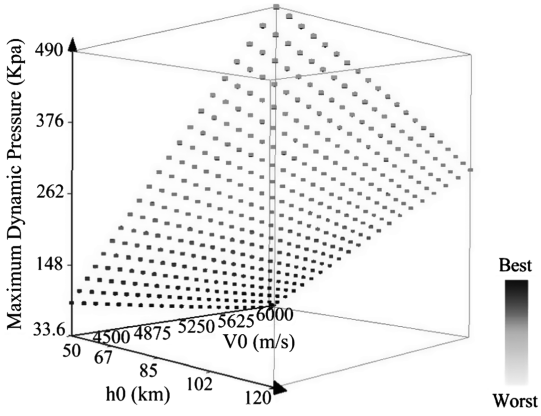

Fig. 20 Experimental design space of fuel-optimal trajectories of the inner loop: maximum dynamic pressure (shade reflects the change of $\bar{q}_{\max}$).

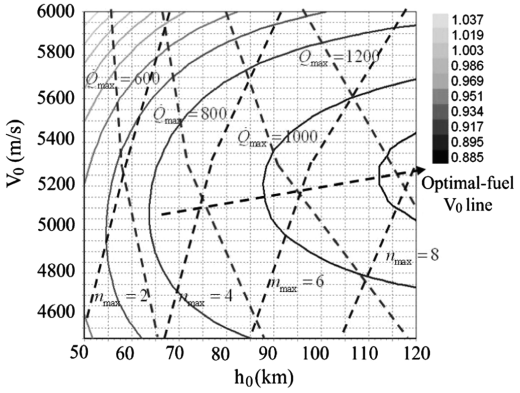

Fig. 21 Contour plot of fuel rate and path constraints.

maximum heating rate line and maximum acceleration load constraint line. There is always a contour curve of fuel rate that crosses the intersection of path constraint lines. There are three possibilities in terms of the relative position of contour curve (which crosses the intersection point) and the path constraint lines:

1) If the vertex of the crossing contour curve is in the feasible area (not at the intersection point), there will be a contour curve with lower fuel rate tangent on one of the two path constraint lines.

2) If the vertex of the crossing contour curve is not in the feasible area, the optimal fuel solution will be at the intersection point.

3) For an extreme case, if the vertex of the contour curve is the intersection point; this point will be fuel-optimal solution.

So the fuel-optimal solution will be either at one path constraint line or at the intersection point. Figure 22 shows that highest velocity will achieve lowest heat load within constraints. These observations can help to reduce the searching area and confirm the result during the process of tradespace visualization.

Different path constraints can be imposed based on the mission requirements. In this example, four different groups of path constraints are imposed based on Figs. 21 and 22: 1) no constraint, 2) $\dot{Q}_{\max} = 800$ W/cm^2 and $n_{\max} = 4$ g, 3) $\dot{Q}_{\max} = 800$ W/cm^2 and $n_{\max} = 3$ g, and 4) $\dot{Q}_{\max} = 500$ W/cm^2 and $n_{\max} = 2$ g. Since each run of the inner loop is an optimization process, the searching process with a genetic algorithm adopting the original model will be too computationally expensive. A way to solve the problem is to use approximation models to replace the original optimization model. The response surface methodology (RSM) is introduced to construct the approximation model.

Metamodeling

Concept

The concept of metamodeling is to use statistical techniques to approximate a detailed analysis model (inner-loop optimization model in this paper) [29]. There are some benefits by using metamodeling technique, as described in [29], and include the following:

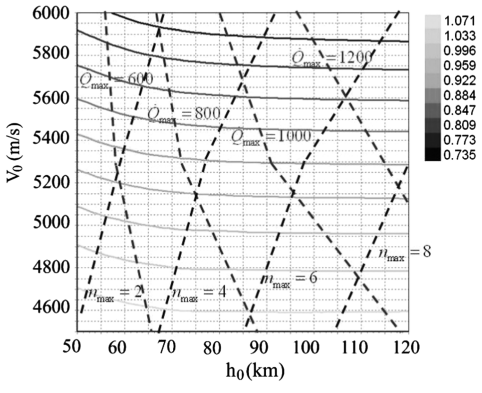

Fig. 22 Contour plot of heat load and path constraints.

1) It provides fast analysis tools for optimization, particularly for genetic algorithm.

2) It can provide insight into the relationship between the input and the output.

Generally, metamodeling techniques involve the follow steps [29]:

1) Choose an experiment design to generate data.

2) Choose a model to represent the data.

3) Fit the model to the observed data.

There are several prevalent methods to construct an approximation model, such as RSM, kriging, or neural networks.

The characteristics of RSM are [30] that it is easy to implement and most well established, and it is appropriate for applications with a small number of inputs (the input variables of the outer-loop optimization are only h_0 and V_0). A third-order response surface model is used to approximate the inner-loop optimization model by RSM in this paper.

Mathematics of Response Surface Methodology

A true model in response surface methodology can be expressed by

$$\boldsymbol{y}(\boldsymbol{x}) = f(\boldsymbol{x}) + \boldsymbol{\varepsilon} \tag{25}$$

where $\boldsymbol{y}(\boldsymbol{x})$ is the unknown function of real model, $f(\boldsymbol{x})$ is a known polynomial function of $\boldsymbol{x}$, and $\boldsymbol{\varepsilon}$ is random error, which is assumed to be normally distributed with zero mean and variance σ^2. A full cubic model for two factors can be expressed as

$$\begin{aligned}\hat{y} = {} & \beta_0 + \beta_1 x_1 + \beta_2 x_2 + \beta_3 x_1 x_2 + \beta_4 x_1^2 + \beta_5 x_2^2 \\ & + \beta_6 x_1^2 x_2 + \beta_7 x_1 x_2^2 + \beta_8 x_1^3 + \beta_9 x_2^3\end{aligned} \tag{26}$$

The coefficients β_i $(i = 0, 1, \ldots, 9)$ determined through a least square regression to minimize the sum of the squares of deviation of predicted value $\hat{\boldsymbol{y}}(\boldsymbol{x})$ from the actual value $y(\boldsymbol{x})$. The experiment data from earlier are used instead of often used central composite designs as sample data [29]. More details on response surface methodologies can be found in [31]. The whole design space is divided into two parts and each part is approximated by a cubic polynomial through the response surface methodology. The approximation models for the objectives and the path constraints are given in Appendix A.

Error Analysis of Approximation Model

The most important concern of an approximation model is that if it is precise enough to represent the original model. Three parameters are used to measure the error of the approximation [18]:

1) The standard error (SE) of regression model is defined as

$$\mathrm{SE} = \sqrt{\sum_{i=1}^{k} (y_i - \hat{y}_i)^2} \tag{27}$$

2) The coefficient of variation is defined as ratio of standard error to the average value of response variable $\bar{\hat{y}}$:

$$\mathrm{COV} = \frac{\mathrm{SE}}{\bar{\hat{y}}} \tag{28}$$

A smaller value of these two parameters indicates better fit.

3) The coefficient of multiple determination R^2 is defined as the ratio of the regression sum of squares to the total sum of squares of the fit (expressed as a percentage). The value closer to 100% indicates better fit:

$$\begin{aligned} R^2 &= \frac{SS_{\mathrm{reg}}}{SS_{\mathrm{tot}}} = \frac{SS_{\mathrm{reg}}}{SS_{\mathrm{reg}} + SS_{\mathrm{err}}} \\ &= \frac{\sqrt{\sum_{i=1}^{k} (\hat{y}_i - \bar{\hat{y}})^2}}{\sqrt{\sum_{i=1}^{k} (\hat{y}_i - \bar{\hat{y}})^2} + \sqrt{\sum_{i=1}^{k} (y_i - \hat{y}_i)^2}} \end{aligned} \tag{29}$$

The errors of sample designs of groups 1–4 are given in Tables B1–B4. It can be seen that the error between the approximation model and the real model are reasonable small, so the approximate model will be used to conduct further analysis. The run time using the approximation model is less than 0.1 s, which compares favorably with the original optimization model at average 31 s (varies from initial states and if the path constraints of the inner loop is imposed).

Generate Pareto Set

We can now start to generate the Pareto set of the solutions with different path constraints by using the approximate model. The results of these four groups are given in Figs. 23–30. The Pareto fronts are given in Figs. 23–26. The points highlighted with black crossing are Pareto solutions in Figs. 27–30. The shade reflects the preference value of the two objectives. Darker points are the better results that have lower fuel rate and heat load.

Figures 23–26 show that the fuel performance and heat performance will be degraded as the stricter path constraints are imposed. Figure 27 shows that if there is no path constraint, the Pareto solutions will be on the highest height (120 km). The optimal fuel-rate solution is on the fuel-optimal velocity line on the highest height (120 km). The optimal heat load solution is on 120 km as well and on the highest velocity (6000 m/s). Only the maximum acceleration load constraint is different in group 2 and group 3. In group 2, the Pareto solutions are on the maximum heating rate constraint line. In group 3, the Pareto solutions are on both of the path constraint lines. The optimal fuel-rate solution is on the intersection point of the two path constraint lines in group 2 and on the maximum acceleration load constraint line in group 3. The optimal heat load solutions of group 2 and group 3 are both on the highest velocity (6000 m/s). In group 4, the Pareto solutions are on the maximum heating rate constraint line. The optimal fuel-rate solution is on the intersection point of the two path constraint lines. The optimal heat load solution is also on the highest velocity.

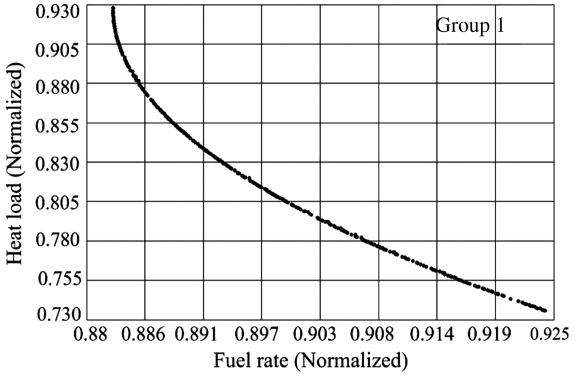

Fig. 23 Pareto front of group 1.

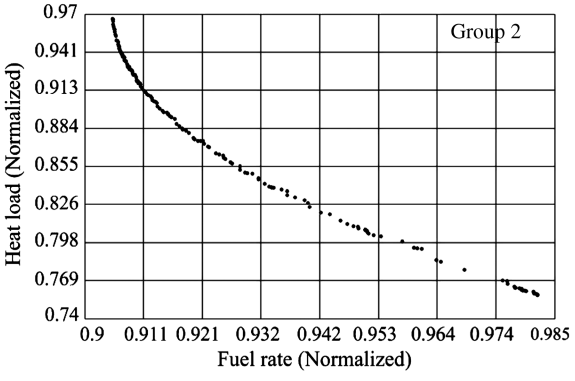

Fig. 24 Pareto front of group 2.

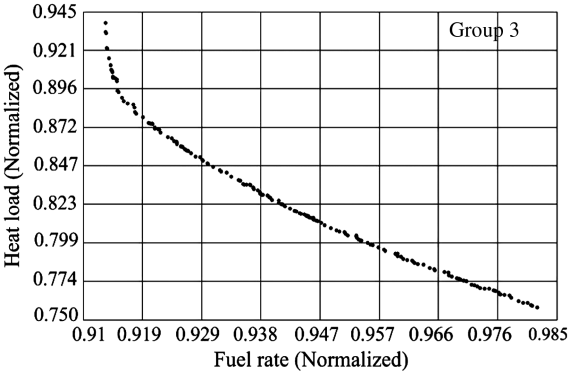

Fig. 25 Pareto front of group 3.

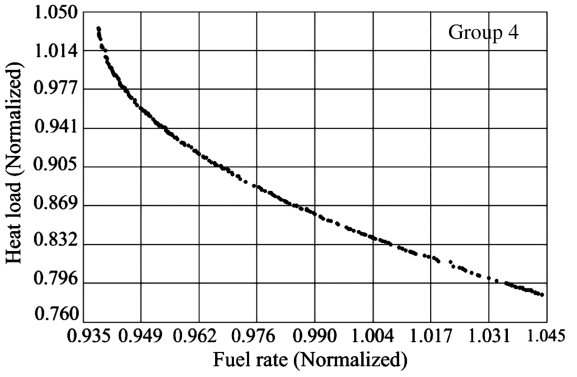

Fig. 26 Pareto front of group 4.

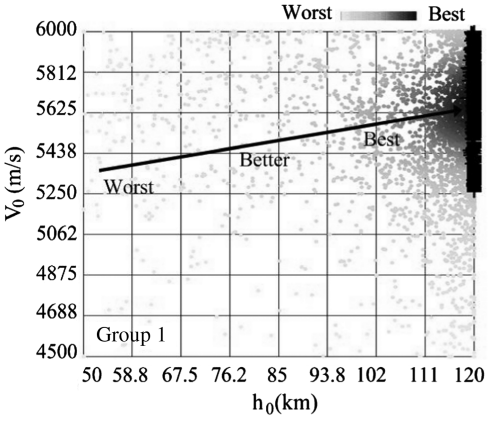

Fig. 27 Optimal initial states of group 1.

The results show that the lower boundary of V_0 of the Pareto solutions is the optimal fuel-rate solution, and the higher boundary of V_0 of the Pareto solutions is the optimal heat load solution. The Pareto solutions are between these two points (optimal fuel-rate solution and optimal heat load solution) along with the constraints (path constraints or maximum height constraints) lines. For the optimal fuel-rate solutions, they are always on one or two of the constraint lines, depending on how strict of the constraints are. The initial velocities of all the optimal heat load solutions are equal to 6000 m/s and always on the maximum heating rate line. The Pareto fronts subject to the different path constraints are visualized through tradespace visualization methods. For periodic cruise trajectories, the fuel rate and heat load are strongly related to the initial states. The path constraints will change the Pareto front. If the designers need to fill any gap on the Pareto front, the search space can be reduced according to the visualization.

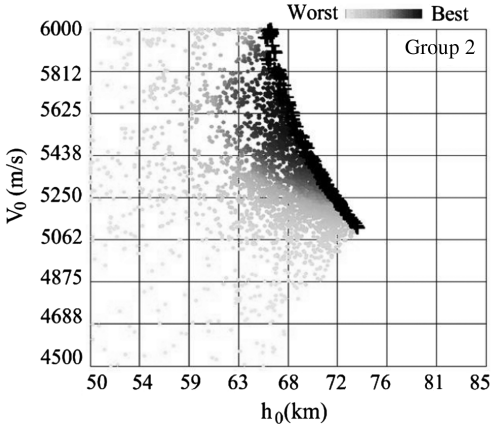

Fig. 28 Optimal initial states of group 2.

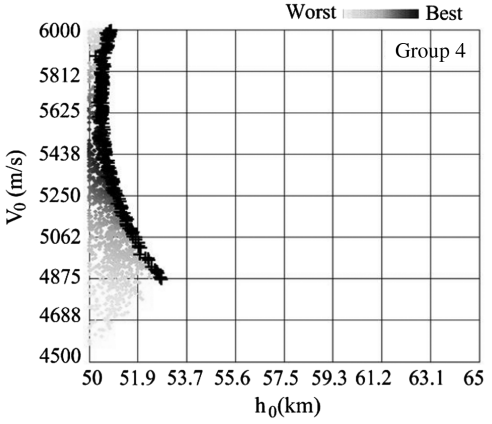

Fig. 30 Optimal initial states of group 4.

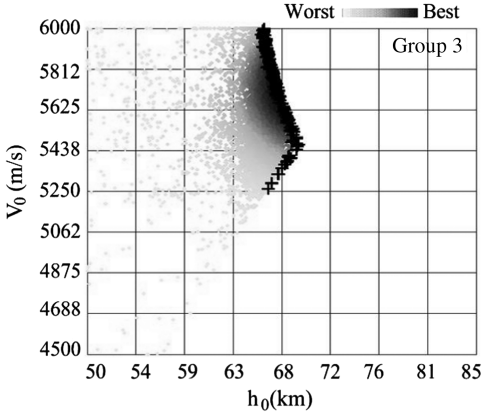

Fig. 29 Optimal initial states of group 3.

Select Preferred Design

The designers can select their preferred designs from the Pareto solutions according to the mission requirements. Here, we show the results of optimal fuel rate, optimal heating load and the best balance results. Table 2 shows the results from approximation model and Table 3 shows the results from real inner-loop optimization model.

The maximum error of all the objectives and path constraints of these solutions from Tables 2 and 3 are as follows: fuel rate is 0.5%, heat load is 0.1%, maximum heating rate is 1.0%, and maximum acceleration load is 0.9%. The errors are reasonably small. Figures 31 and 32 only show the height histories and the optimal angle of attack of groups 3 and 4.

Figure 31 shows that the optimal heat solutions (groups 3-b and 4-b) have a higher lowest flight height and experience a thinner atmosphere. Since the only objective of the inner loop is fuel rate, the optimal control histories in Fig. 32 are actually the fuel-optimal control histories. The discontinuities points of angle of attack are at the switch point of the engine.

Pareto Set with Inner-Loop Active Path Constraints

As mentioned earlier, small constraints imposed on control variables will not degrade the fuel-rate performance (the inner-loop objective) significantly and widen the search space (also improve the heat performance). The results from groups 2–4 (see Figs. 28–30) indicate that the Pareto solutions are on the border where the path constraints have no impact on control variables. The results of groups 2–4 are only near-optimal solutions, since the effect on the path constraints from control variables is ignored. So in group 5, we let the control variables in the inner loop achieve the total path constraints that are the same as group 2: namely, $\dot{Q}_{\max} =$

Table 2 Results from approximation model of the selected preferred Pareto solutions

Objective preference	Fuel rate, normalized	Heat load, normalized	Maximum heating rate, W/cm^2	Maximum acceleration load, g	Optimal h_0, km	Optimal V_0, m/s
			OSC Group			
Optimal fuel rate	1	1	321.1	0.60	43.04	4948
			Group 1: no constraint			
a: optimal fuel rate	0.883	0.927	1250.0	8.02	120.0	5262
b: optimal heat load	0.924	0.736	1427.3	6.15	120.0	6000
c: best balance	0.894	0.828	1354.0	7.05	120.0	5661
			Group 2: $\dot{Q}_{\max} = 800$, $n_{\max} = 4$			
a: optimal fuel rate	0.905	0.966	799.1	3.99	73.57	5116
b: optimal heat load	0.982	0.758	799.7	1.90	65.93	6000
c: best balance	0.933	0.842	799.7	2.53	67.55	5662
			Group 3: $\dot{Q}_{\max} = 800$, $n_{\max} = 3$			
a: optimal fuel rate	0.914	0.938	734.2	3.00	66.28	5261
b: optimal heat load	0.982	0.758	799.7	1.90	65.93	6000
c: best balance	0.938	0.829	800.0	2.42	67.23	5714
			Group 4: $\dot{Q}_{\max} = 500$, $n_{\max} = 2$			
a: optimal fuel rate	0.939	1.035	499.3	1.98	52.78	4874
b: optimal heat load	1.044	0.786	499.4	0.71	50.83	6000
c: best balance	0.965	0.909	499.8	1.10	50.63	5481

Table 3 Results from original model of the selected preferred Pareto solutions

Objective preference	Fuel rate, normalized	Heat load, normalized	Maximum heating rate, W/cm^2	Maximum acceleration load, g	Optimal h_0, km	Optimal V_0, m/s
			Group 1: no constraint			
a: optimal fuel rate	0.883	0.928	1249.1	8.01	120.0	5262
b: optimal heat load	0.925	0.735	1425.4	6.14	120.0	6000
c: best balance	0.893	0.828	1355.6	7.05	120.0	5661
			Group 2: $\dot{Q}_{\max} = 800$, $n_{\max} = 4$			
a: optimal fuel rate	0.905	0.967	799.8	4.00	73.57	5116
b: optimal heat load	0.982	0.757	799.6	1.90	65.93	6000
c: best balance	0.933	0.842	799.9	2.53	67.55	5662
			Group 3: $\dot{Q}_{\max} = 800$, $n_{\max} = 3$			
a: optimal fuel rate	0.915	0.938	731.3	3.01	66.28	5261
b: optimal heat load	0.982	0.757	799.6	1.90	65.93	6000
c: best balance	0.938	0.829	800.0	2.41	67.23	5714
			Group 4: $\dot{Q}_{\max} = 500$, $n_{\max} = 2$			
a: optimal fuel rate	0.939	1.035	500.0	1.97	52.78	4874
b: optimal heat load	1.049	0.786	494.7	0.71	50.83	6000
c: best balance	0.965	0.909	499.5	1.11	50.63	5481

800 W/cm^2, and $n_{\max} = 4\ g$. We can repeat the process of aforementioned tradespace visualization to generate the Pareto front of group 5. A full factorial experiment (2 levels, 21 factors) that the path constraints are imposed in the inner loop is conducted. The searching space is given as the range of h_0 is 60–90 km (higher altitude will not generate feasible solutions). The range of V_0 is from 4950 to 6000 m/s. The constraints $\bar{J}_1 \leq 1$ and $\bar{J}_2 \leq 1$ are imposed. The results are given in Figs. 33–36.

Figures 35 and 36 show the active path constraints region (reach the maximum value of the path constraints) of the inner loop of group 5. The approximation models then can be constructed from RSM (models III and IV in Appendix A). The Pareto fronts and optimal initial states of group 5 are generated by the approximation models. The results are given in Figs. 37 and 38.

The borders (approximate) of the active path constraints are shown in Fig. 38. Note that the borders of active path constraints in Fig. 38 are not the path constraint lines in the outer loop (see Figs. 21 and 22). The reason for that is $\dot{Q}_{\max}$ and $n_{\max}$ are related (imposing one will reduce the value of the other one). The whole design space is divided into four parts by the borders of the path constraints: namely, regions 1, 2, 3, and 4. There are four possibilities in terms of whether the path constraints are activated on the control variables:

1) If the solutions are in region 1, no path constraints are activated on the control variables.

2) If the solutions are in region 2, $\dot{Q}_{\max}$ is activated on the control variables and $n_{\max}$ is satisfied automatically.

3) If the solutions are in region 3, $n_{\max}$ is activated on the control variables and $\dot{Q}_{\max}$ is satisfied automatically.

4) If the solutions are in region 4, both $\dot{Q}_{\max}$ and $n_{\max}$ are activated on the control variables.

It can be seen that the Pareto solutions of group 5 are in region 2 for most points and region 4 for only a few points near the fuel-rate optimal solution. Table 4 shows the optimal fuel rate, optimal heat

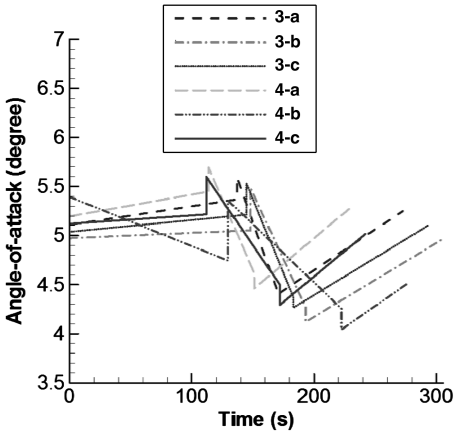

Fig. 32 Angle of attack of groups 3 and 4 from Table 3.

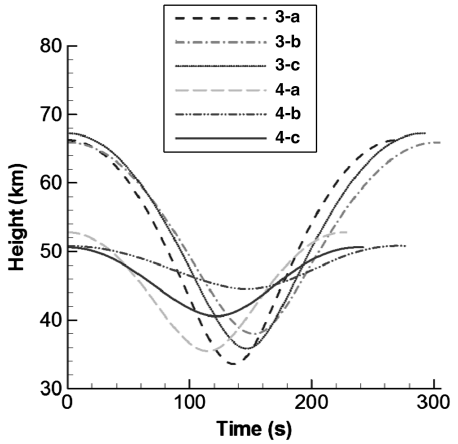

Fig. 31 Height of groups 3 and 4 from Table 3.

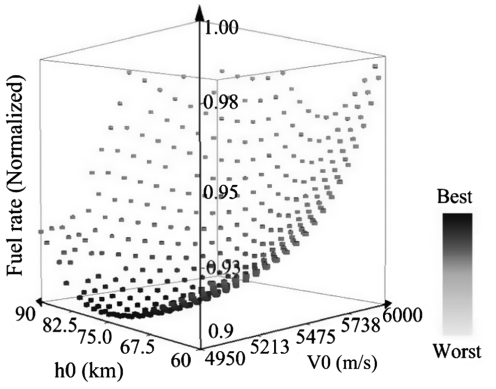

Fig. 33 Experimental design space of group 5: fuel rate (shade reflects the change of fuel rate).

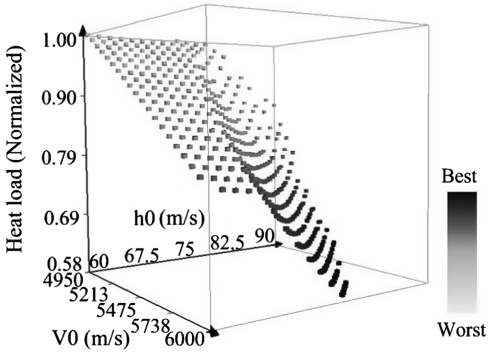

Fig. 34 Experimental design space of group 5: heat load (shade reflects the change of heat load).

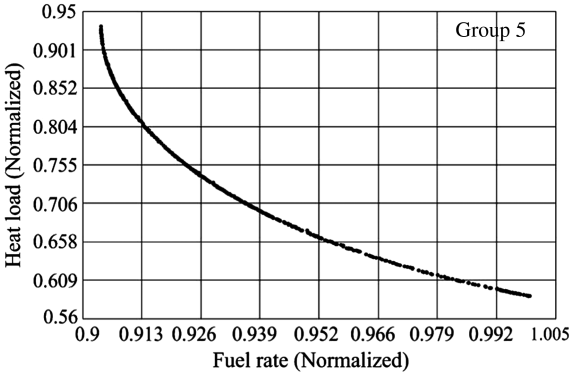

Fig. 37 Pareto front of group 5.

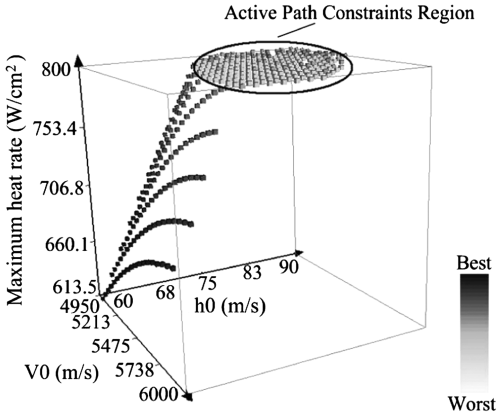

Fig. 35 Experimental design space of group 5: maximum heat rate (shade reflects the change of $\dot{Q}_{\max}$).

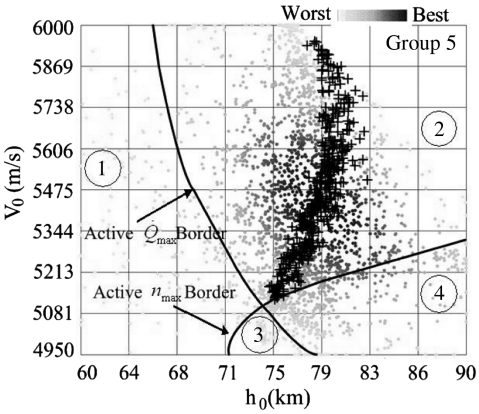

Fig. 38 Optimal initial states of group 5.

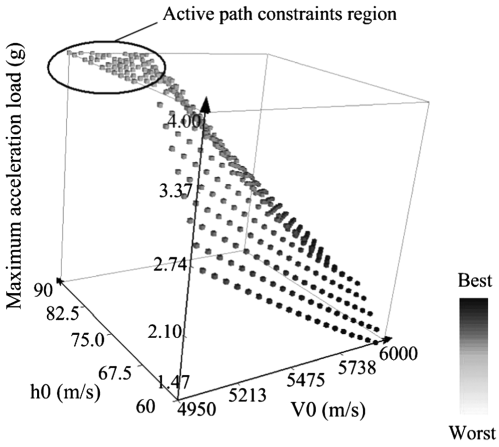

Fig. 36 Experimental design space of group 5: maximum acceleration load (shade reflects the change of $n_{\max}$).

load, and best balance solutions of group 5 with original inner-loop optimization model.

Table 4 shows that the optimal fuel-rate solution is in region 4 and the other two solutions are in region 2. Compare the results from group 2 (see Table 3) and group 5 (see Table 4), the results from group 5 are generally better than the ones from group 2. This is because group 5 provides the solutions in which the path constraints were activated on control variables (inner loop) that are the true optimal solutions subject to constraints. However, the optimal fuel-rate solutions are very close for these two groups, which shows that imposing path constraints only in outer loop can generate the near fuel-optimal solutions. The heat performance is significantly better (higher altitude) when path constraints are imposed on control variables (group 5).

Note that the results of groups 1–5 show that a higher h_0 and V_0 desirable for cruise phase, but it also costs more energy to get to a higher start condition. So the overall optimal solutions include ascent trajectory phase need to be investigated as a follow-on work.

Table 4 Results from group 5 with original model

Objective preference	Fuel rate, normalized	Heat load, normalized	Maximum heating rate, W/cm²	Maximum acceleration load, g	Optimal h_0, km	Optimal V_0, m/s
			Group 5: $\dot{Q}_{\max} = 800$, $n_{\max} = 4$			
a: optimal fuel rate	0.904	0.934	800.0	4.00	75.12	5125
b: optimal heat load	0.998	0.585	800.0	2.29	78.34	5946
c: best balance	0.955	0.660	800.0	2.99	80.30	5618

Conclusions

The genetic algorithm and a sequential quadratic programming algorithm are used to study the multi-objective optimal periodic cruise trajectories. The individual effects on the objectives and constraints from both initial states and control variables are studied. The results show that the initial states are key parameters to determine fuel-optimal solutions subject to different path constraints.

The two-level optimization method makes incorporating a genetic algorithm (dealing with the initial states) and local algorithms (dealing with the control variables) possible. With the advantage of a genetic algorithm (used in the tradespace visualization), the entire families of optimal solutions with different constraints can be found, with these Pareto solutions offering the designer more choices. Compared with the optimization-based design process using an evolutionary algorithm, the tradespace visualization allows the designers to properly formulate the problem (specify appropriate objectives and constraints) and to be more confident with the optimality of the solutions. Another advantage of the two-level optimization method, as long as the outputs of different inner-loop models are reasonably close, is that the inner-loop model is replaceable without affecting the outer loop. Thus, once the experimental design spaces are generated from the inner-loop optimization model, the approximation model can be introduced to speed up the optimization process.

Appendix A: Approximation Models from Response Surface Methodology

Model I (groups 1–4), $h_0 \geq 85$ km:

$$\begin{aligned}\hat{\tilde{J}}_1 &= -0.6092551 - 0.2138189 \times 10^{-5} \times h_0 + 0.1213680 \times 10^{-2} \\ &\times V_0 + 0.2199958 \times 10^{-9} \times h_0 \times V_0 + 0.1103069 \times 10^{-10} \\ &\times h_0^2 - 0.2909753 \times 10^{-6} \times V_0^2 + 0.3639336 \times 10^{-14} \\ &\times h_0^2 \times V_0 + 0.1103069 \times 10^{-10} \times h_0^2 - 0.2909753 \times 10^{-6} \\ &\times V_0^2 + 0.3639336 \times 10^{-14} \times h_0^2 \times V_0 - 0.1134646 \times 10^{-12} \\ &\times V_0^2 \times h_0 - 0.7741788 \times 10^{-16} \times h_0^3 + 0.2303371 \times 10^{-10} \\ &\times V_0^3 \end{aligned} \tag{A1}$$

$$\begin{aligned}\hat{\tilde{J}}_2 &= 0.8628225 - 0.1244635 \times 10^{-5} \times h_0 + 0.3563840 \times 10^{-3} \\ &\times V_0 + 0.1708186 \times 10^{-10} \times h_0 \times V_0 + 0.1281772 \times 10^{-10} \\ &\times h_0^2 - 0.7928315 \times 10^{-7} \times V_0^2 + 0.1023877 \times 10^{-14} \\ &\times h_0^2 \times V_0 - 0.3522263 \times 10^{-13} \times V_0^2 \times h_0 - 0.5290142 \times 10^{-16} \\ &\times h_0^3 + 0.3224057 \times 10^{-11} \times V_0^3 \end{aligned} \tag{A2}$$

$$\begin{aligned}\hat{\tilde{Q}}_{\max} &= 0.1368107 \times 10^4 - 0.9421702 \times 10^{-2} \times h_0 - 0.8560719 \\ &\times V_0 + 0.8460459 \times 10^{-5} \times h_0 \times V_0 - 0.6518356 \times 10^{-7} \\ &\times h_0^2 + 0.1487072 \times 10^{-3} \times V_0^2 - 0.1670244 \times 10^{-10} \\ &\times h_0^2 \times V_0 - 0.2624390 \times 10^{-9} \times V_0^2 \times h_0 \\ &+ 0.3823875 \times 10^{-12} \times h_0^3 - 0.1048187 \times 10^{-7} \times V_0^3 \end{aligned} \tag{A3}$$

$$\begin{aligned}\hat{n}_{\max} &= 0.6669090 + 0.1238728 \times 10^{-3} \times h_0 - 0.1208974 \times 10^{-2} \\ &\times V_0 + 0.1355299 \times 10^{-7} \times h_0 \times V_0 - 0.1707872 \times 10^{-9} \\ &\times h_0^2 + 0.1664279 \times 10^{-6} \times V_0^2 - 0.1979948 \times 10^{-12} \\ &\times h_0^2 \times V + 0.9133976 \times 10^{-12} \times V_0^2 \times h_0 \\ &+ 0.3679668 \times 10^{-14} \times h_0^3 - 0.3372903 \times 10^{-10} \times V_0^3 \end{aligned} \tag{A4}$$

Model II (groups 1–4), $h_0 < 85$ km:

$$\begin{aligned}\hat{\tilde{J}}_1 &= -0.7877075 - 0.1334702 \times 10^{-4} \times h_0 + 0.1488602 \times 10^{-2} \\ &\times V_0 + 0.2954448 \times 10^{-8} \times h_0 \times V_0 + 0.6618182 \times 10^{-10} \\ &\times h_0^2 - 0.3653964 \times 10^{-6} \times V_0^2 + 0.3148363 \times 10^{-13} \\ &\times h_0^2 \times V - 0.7964268 \times 10^{-12} \times V_0^2 \times h_0 \\ &- 0.9338642 \times 10^{-15} \times h_0^3 + 0.3126214 \times 10^{-10} \times V_0^3 \end{aligned} \tag{A5}$$

$$\begin{aligned}\hat{\tilde{J}}_2 &= 0.9197741 - 0.8492234 \times 10^{-5} \times h_0 + 0.4301396 \times 10^{-3} \\ &\times V_0 + 0.8134856 \times 10^{-9} \times h_0 \times V_0 + 0.7560975 \times 10^{-10} \\ &\times h_0^2 - 0.9829531 \times 10^{-7} \times V_0^2 + 0.5509288 \times 10^{-14} \\ &\times h_0^2 \times V_0 - 0.1937018 \times 10^{-12} \times V_0^2 \times h_0 \\ &- 0.3835204 \times 10^{-15} \times h_0^3 + 0.5236912 \times 10^{-11} \times V_0^3 \end{aligned} \tag{A6}$$

$$\begin{aligned}\hat{\tilde{Q}}_{\max} &= 0.9634054 \times 10^3 - 0.584777 \times 10^{-2} \times h_0 \\ &- 0.6918555 \times V_0 + 0.8791102 \times 10^{-5} \times h_0 \\ &\times V_0 - 0.1220364 \times 10^{-6} \times h_0^2 + 0.1174547 \times 10^{-3} \\ &\times V_0^2 - 0.6418627 \times 10^{-10} \times h_0^2 \times V_0 + 0.4118066 \times 10^{-9} \\ &\times V_0^2 \times h_0 + 0.1690484 \times 10^{-11} \times h_0^3 - 0.1199248 \times 10^{-7} \\ &\times V_0^3 \end{aligned} \tag{A7}$$

$$\begin{aligned}\hat{n}_{\max} &= 0.6837498 + 0.1330069 \times 10^{-3} \times h_0 \\ &- 0.1923996 \times 10^{-2} \times V_0 + 0.5870633 \times 10^{-7} \times h_0 \\ &\times V_0 - 0.1667477 \times 10^{-8} \times h_0^2 - 0.1056736 \times 10^{-6} \\ &\times V_0^2 + 0.4574384 \times 10^{-12} \times h_0^2 \times V - 0.1350685 \times 10^{-10} \\ &\times V_0^2 \times h_0 - 0.4526531 \times 10^{-14} \times h_0^3 + 0.6129930 \times 10^{-10} \\ &\times V_0^3 \end{aligned} \tag{A8}$$

Model III (group 5), $h_0 \geq 72$ km:

$$\begin{aligned}\hat{\tilde{J}}_1 &= -0.5664927 \times 10^1 + 0.2815108 \times 10^{-3} \times h_0 \\ &+ 0.8236505 \times 10^{-3} \times V_0 - 0.7134605 \times 10^{-7} \times h_0 \\ &\times V_0 - 0.1606637 \times 10^{-8} \times h_0^2 + 0.2094365 \times 10^{-6} \\ &\times V_0^2 + 0.3295699 \times 10^{-12} \times h_0^2 \times V_0 + 0.2473752 \times 10^{-11} \\ &\times V_0^2 \times h_0 + 0.4039297 \times 10^{-15} \times h_0^3 - 0.1745707 \times 10^{-10} \\ &\times V_0^3 \end{aligned} \tag{A9}$$

$$\begin{aligned}\hat{\tilde{J}}_2 &= -0.7661653 \times 10^2 + 0.1346142 \times 10^{-2} \times h_0 \\ &+ 0.2536153 \times 10^{-1} \times V_0 - 0.4492167 \times 10^{-8} \\ &\times h_0^2 - 0.3744578 \times 10^{-6} \times h_0 \times V_0 - 0.2170709 \times 10^{-5} \\ &\times V_0^2 + 0.6755879 \times 10^{-12} \times h_0^2 \times V_0 + 0.2454104 \times 10^{-10} \\ &\times V_0^2 \times h_0 + 0.4232803 \times 10^{-14} \times h_0^3 + 0.2392278 \times 10^{-10} \\ &\times V_0^3 \end{aligned} \tag{A10}$$

Model IV (group 5): $h_0 < 72$ km

$$\hat{\tilde{J}}_1 = -0.1275256 \times 10^2 + 0.2700968 \times 10^{-3} \times h_0 + 0.4755546 \times 10^{-2} \times V_0 - 0.3549114 \times 10^{-7} \times h_0 \times V_0 - 0.2727996 \times 10^{-8} \times h_0^2 - 0.7389615 \times 10^{-6} \times V_0^2 + 0.2440872 \times 10^{-12} \times h_0^2 \times V_0 + 0.2506847 \times 10^{-12} \times V_0^2 \times h_0 + 0.7546121 \times 10^{-14} \times h_0^3 + 0.4986385 \times 10^{-10} \times V_0^3 \quad \text{(A11)}$$

$$\hat{\tilde{J}}_2 = 0.3993517 \times 10^2 - 0.1665742 \times 10^{-2} \times h_0 - 0.2147942 \times 10^{-2} \times V_0 + 0.1638961 \times 10^{-7} \times h_0^2 + 0.2360921 \times 10^{-6} \times h_0 \times V_0 - 0.9627323 \times 10^{-6} \times V_0^2 - 0.1460136 \times 10^{-11} \times h_0^2 \times V_0 - 0.4905021 \times 10^{-11} \times V_0^2 \times h_0 - 0.4518998 \times 10^{-13} \times h_0^3 + 0.7510255 \times 10^{-10} \times V_0^3 \quad \text{(A12)}$$

Appendix B: Errors of the Approximation Models

Table B1 Maximum error of the approximation model I

Response	SE	COV	R^2
Fuel rate (normalized)	0.00043	0.05%	99.90%
Heat load (normalized)	0.0024	0.03%	100.0%
Maximum heating rate	0.78	0.07%	100.0%
Maximum acceleration load	0.013	0.20%	99.99%

Table B2 Maximum error of the approximation model II

Response	SE	COV	R^2
Fuel rate (normalized)	0.00088	0.09%	99.90%
Heat load (normalized)	0.00048	0.05%	100.0%
Maximum heating rate	1.51	0.21%	99.99%
Maximum acceleration load	0.01	0.31%	99.99%

Table B3 Maximum error of the approximation model III

Response	SE	COV	R^2
Fuel rate (normalized)	0.0014	0.15%	99.77%
Heat load (normalized)	0.0053	0.69%	99.80%

Table B4 Maximum error of the approximation model IV

Response	SE	COV	R^2
Fuel rate (normalized)	0.00051	0.05%	99.95%
Heat load (normalized)	0.0045	0.52%	99.74%

Acknowledgments

This work is partly supported by the National Science Foundation under grant no. CMMI-0620948. Any opinions, findings, and conclusions or recommendations presented in this paper are those of the authors and do not necessarily reflect the views of the National Science Foundation. The first author also would like to thank the Chinese Scholarship Council, who sponsored his studies at Pennsylvania State University. We would also like to thank Patrick Reed and Timothy Simpson and Chad Kasell from Pennsylvania State University and Taurik Elgabrowny from Phoenix Integration, Inc.

References

[1] Edelbaum, T., "Maximum Range Flight Paths," United Aircraft Corp., Rept. R-22465-24, Moscow, 1955.

[2] Speyer, J. L., "Nonoptimality of the Steady-State Cruise for Aircraft," *AIAA Journal*, Vol. 14, No. 11, 1976, pp. 1604–1610. doi:10.2514/3.7257

[3] Speyer, J. L., "Periodic Optimal Flight," *Journal of Guidance, Control, and Dynamics*, Vol. 19, No. 4, 1996, pp. 745–755. doi:10.2514/3.21695

[4] Chuang, C., and Morimoto, H., "Periodic Optimal Cruise for a Hypersonic Vehicle with Constraints," *Journal of Spacecraft and Rockets*, Vol. 34, No. 2, 1997, pp. 165–171. doi:10.2514/2.3205

[5] Carter, P. H., Pines, D. J., and Rudd, L. V., "Approximate Performance of Periodic Hypersonic Cruise Trajectories for Global Reach," *Journal of Aircraft*, Vol. 35, No. 6, 1998, pp. 857–867. doi:10.2514/2.2405

[6] Breakwell, J., and Schoaee, H., "Minimum Fuel Flight Paths for a Given Range," AIAA Paper 1980-1660, 1980.

[7] Dewell, L. D., and Speyer, J. L., "An Investigation of the Fuel-Optimal Periodic Trajectories for a Hypersonic Vehicle," AIAA Paper 1993-3753, 1993.

[8] Dewell, L. D., and Speyer, J. L., "Fuel-Optimal Periodic Control and Regulation in Constrained Hypersonic Flight," *Journal of Guidance, Control, and Dynamics*, Vol. 20, No. 5, 1997, pp. 923–932. doi:10.2514/2.4136

[9] Grimm, W., Well, K. H., and Oberle, H. J., "Periodic Control for Minimum-Fuel Aircraft Trajectories," *Journal of Guidance, Control, and Dynamics*, Vol. 9, No. 2, 1986, pp. 169–174. doi:10.2514/3.20086

[10] Anhtuan, D. N., "A Fuel-Optimal Trajectory for a Constrained Hypersonic Using a Direct Transcription Method," *IEEE Aerospace Conference Proceedings*, Vol. 4, IEEE, Piscataway, NJ, 2004, pp. 2704–2709.

[11] Rankins, F., and Pines, D. J., "Relative Heat Load Comparison of Vehicles Flying Hypersonic Transatmosphere Trajectory," *Journal of Spacecraft and Rockets*, Vol. 37, No. 4, 2000, pp. 491–498. doi:10.2514/2.3590

[12] Chen, R. H., Williamson, W. R., Speyer, J. L., Youssef, H., and Chowdhry, R., "Optimization and Implementation of Periodic Cruise for a Hypersonic Vehicle," *Journal of Guidance, Control, and Dynamics*, Vol. 29, No. 5, 2006, pp. 1032–1040. doi:10.2514/1.19361

[13] Betts, J. T., "Survey of Numerical Methods for Trajectory Optimization," *Journal of Guidance, Control, and Dynamics*, Vol. 21, No. 2, 1998, pp. 193–207. doi:10.2514/2.4231

[14] Biegler, L. T., "An Overview of Simultaneous Strategies for Dynamic Optimization," *Chemical Engineering and Processing*, Vol. 46, No. 11, 2007, pp. 1043–1053. doi:10.1016/j.cep.2006.06.021

[15] Balling, R., "Design by Shopping: A New Paradigm?," *Proceedings of the Third World Congress of Structural and Multidisciplinary Optimization (WCSMO-3)*, Vol. 1, International Society for Structural and Multidisciplinary Optimization (ISSMO), Daejeon, ROK, 1999, pp. 295–297.

[16] Simpson, T. W., Spencer, D. B., Yukish, M. A., and Stump, G., "Visual Steering Commands and Test Problems to Support Research in Tradespace Exploration," AIAA Paper 2008-6085, 2008.

[17] Stump, G., Lego, S., Yukish, M., Simpson, T. W., and Donndelinger, J. A., "Visual Steering Commands for Tradespace Exploration: User-Guided Sampling with Example," ASME Design Engineering Technical Conference—Design Automation Conference, American Society of Mechanical Engineers, Paper DETC2007/DAC-34684, 2007.

[18] "User Manual of ModelCenter 7.1," Phoenix Integration, Blacksburg, VA, 2007.

[19] Kim, H. M., and Ragon, S., "Interactive Design Selection Process Through Visualization and User Guided Search," AIAA Paper 2006-6952, 2006.

[20] Goldberg, D. E., *Genetic Algorithms in Search, Optimization, and Machine Learning*, Addison Wesley, Reading, MA, 1989.

[21] Deb, K., *Multi-Objective Optimization Using Evolutionary Algorithms*, Wiley, New York, 2001.

[22] Vavrina, M. A., and Howell, K. C., "Global Low-Thrust Trajectory Optimization Through Hybridization of a Genetic Algorithm and a Direct Method," AIAA Paper 2008-6614, 2008.

[23] Subbarao, K., and Shippey, B., "Hybrid Genetic Algorithm Collocation Method for Trajectory Optimization," *Journal of Guidance, Control, and Dynamics*, Vol. 32, No. 4, July–Aug. 2009, pp. 1396–1403.
doi:10.2514/1.41449

[24] Yokoyama, N., and Suzuki, S., "Modified Genetic Algorithm for Constrained Trajectory Optimization," *Journal of Guidance, Control, and Dynamics*, Vol. 28, No. 1, Jan.–Feb. 2005, pp. 139–144.
doi:10.2514/1.3042

[25] Hartmann, J. W., Coverstone-Carroll, V., and Williams, S. N., "Optimal Interplanetary Spacecraft Trajectories via a Pareto Genetic Algorithm," *Journal of the Astronautical Sciences*, Vol. 46, No. 3, 1998, pp. 267–282.

[26] Lawrence, C. T., and Tits, A. L., "A Computationally Efficient Feasible Sequential Quadratic Programming Algorithm," *SIAM Journal on Optimization*, Vol. 11, No. 4, 2001, pp. 1092–1118.
doi:10.1137/S1052623498344562

[27] Soremekun, G., Gürdal, Z., Haftka, R. T., and Watson, L. T., "Composite Laminate Design Optimization by Genetic Algorithm with Generalized Elitist Selection," *Computers and Structures*, Vol. 79, No. 2, 2001, pp. 131–143.
doi:10.1016/S0045-7949(00)00125-5

[28] Suwal, K. R., and Cliff, E. M., "Singular Periodic Solutions in Aircraft Cruise Dash Optimization," AIAA Paper 1990-3369, 1990.

[29] Simpson, T. W., Peplinski, J., Koch, P. N., and Allen, J. K., "On the Use of Statistics in Design and the Implications for Deterministic Computer Experiments," ASME Design Engineering Technical Conference, Sacramento, CA, American Society of Mechanical Engineers, Paper DETC97/DTM-3881, 1997.

[30] Simpson, T. W., Peplinski, J., Koch, P. N., and Allen, J. K., "Metamodels for Computer-Based Engineering Design: Survey and Recommendations," *Engineering with Computers*, Vol. 17, No. 2, 2001, pp. 129–150.
doi:10.1007/PL00007198

[31] Myers, R. H., and Montgomery, D. C., *Response Surface Methodology: Process and Product in Optimization Using Designed Experiments*, 2nd ed., Wiley, New York, 2002.

C. Kluever
Associate Editor